Mathematical Biology and Bioinformatics
2017. V. 12. No 1. P. 14–54. URL: doi:10.17537/2017.12.14

========== **REVIEW ARTICLES** ==========

UDC 530.1: 537.226.4 + 541.1 + 577

Computational Studies of the Hydroxyapatite Nanostructures, Peculiarities and Properties

Bystrov V.S.*

Institute of Mathematical Problems of Biology RAS – the Branch of Keldysh Institute of Applied Mathematics RAS, Pushchino142290, Russia

Abstract. In this review paper the main approaches to modeling the hydroxyapatite (HAP) structures and first-principle calculations of their properties, pure and with various defects, are considered. First, the HAP nano-particles (NPs) and clusters peculiarities are described using different methods: molecular mechanical and quantum mechanical, especially semi-empirical such as PM3. Both approximations used here, namely, restricted Hartee-Fock (RHF) and unrestricted Hartee-Fock (UHF), are considered. The influence of the protons (hydrogens), contained in the surrounding medium (pH), on the formation of HAP nanoparticles of various sizes and shapes is considered and discussed. Second, the HAP crystal unit cells studies are considered on the basis of a density functional theory (DFT) modelling. The main peculiarities of both phases (hexagonal and monoclinic) are considered too, including their ordered and disordered substructures. One of the important aspects of the computer modeling of HAP is to build the models and consider various structural modifications of HAP (such as, vacancies of oxygen atoms and hydroxyl OH group, hydrogen interstitials and different substitutions of atoms in HAP unit cell), which allow explicitly creating and exploring the changes in the charges of HAP and the electrical potential on the HAP surface. HAP modifications are most close to biological HAP and therefore are necessary for implant medical applications and can create and functionalize HAP surface with most adhesive properties for living cells (osteoblasts, osteoclatst). This improves the HAP implant quality. Besides, it has recently been established that oxygen vacancy in HAP influences their photo-catalytic properties. It is important for HAP usage as in environmental remediation and for bacteria inactivation. Therefore it is very important to create and investigate the oxygen vacancy models in HAP, and others defects models. In this work we review a DFT modelling and studies of HAP, both pure perfect bulk and imperfect bulk cases. Special HAP modelling approaches are used for layered slab super-cells units, which include vacuum spaces between the layered slabs forming HAP surface. To all these computer studies the first principle calculations were applied. In this review various DFT approximations are analysed for bulk and surface modified HAP. These approximations are carried out using both the local basis (local density approximation – LDA, in AIMPRO codes) and the plane-waves (generalized gradient approximation – GGA, in VASP codes). Data of all structures and models of HAP defects investigated are widely analyzed.

***Key words*:** *hydroxyapatite, nanostructure, computer modeling, first-principle calculations, bulk crystal, clusters, defects, surface, physical properties, quantum-chemical and semi-empirical approaches, density functional theory.*

*vsbys@mail.ru

INTRODUCTION

Hydroxyapatite (HAP) $Ca_{10}(PO_4)_6(OH)_2$ is one of the essential mineral components in human bone and widely used biomaterials in medicine for implants preparation and insertion [1–3]. It has specific structural features that define its basic physical properties, charge distribution and surface electric potential, which have especially important role for the living cells adhesion and proliferation [1–3]. The specific feature of HAP is that it has a selected direction of the formation of hydroxyl OH groups (inner OH-channels) along the *c* axis, which allows the transfer of protons along this axis under special conditions [4–15]. Special interest here is connected with the physical properties of the nanosized HAP clusters [12–21].

Recent modeling and computational study of HAP structures, their specific surface properties and changes during the formation of various stoichoimetric HAP contents or possible defects [7, 9], to determine the electric potential of the HAP surface charge density (polarization), is an important and necessary task for the study of these properties for HAP nanoparticles with various sizes and shapes [11]. It is also useful for creating of new HAP nanostructures having wide biomedical applications [13–19]. The results of these studies [7, 9, 11, 19–35] allow us to clarify possible mechanisms of structural changes and electrical properties of HAP in the bulk crystal and on the crystal surface (electrical potential, charges and polarization). And this, in turn, will allow one to improve the efficiency of HAP interactions with the living bone cells (osteoblasts, osteoclasts, etc.) and thus to control the quality of the bone implants [11, 14, 15, 19].

It is important to note that all the types of HAP – in the body of the living organisms – are a biological, rather than mineral material. This means that their structure differs from the perfect crystal structure of ordinary minerals. Their difference from an ideal mineral consists primarily in stoichiometry and defects, particularly, such as oxygen O and OH group's vacancies, interstitials of hydrogen H, various atomic impurities and substitutions of several atoms, which change the surface charges and electric potential. Now it is clear that the influence of surface charge and electric potential of the HAP surface on the osteo adhesion of the living cells and their growth, i.e., bone regeneration activity, is very high and important. Studies have shown that the creation of such surface charges (or HAP polarization) increases the adhesion of the osteoblasts cells and enhances their reproduction and growth. According to [34–38], it is especially noticeable for the negatively charged surfaces of HAP.

In this review article we consider, firstly, the model developed for HAP nanoparticles (NPs), based on cluster approach. Second, we investigate the HAP surface charges (polarization) distribution and changes of electron work function following from this model in comparison with experimental data obtained. The influence of additional protons, which saturate the broken bonds, is studied too. Third, we explore the HAP crystal structure model with vacancy (H, O, OH) and interstitial (e.g., additional protons embedded inside HAP structure), and corresponding HAP cluster models, enabling one to compute changes in the electron work function in comparison with photoelectron emission data.

Physical properties of HAP NPs urgent for nanoscience and nanomedicine were explored computationally and experimentally in this work. Special interest is focused on the study of their interfaces under various environmental conditions, connected with changes of HAP surface charges (such as, the influence of protons content, changes in pH, influence of the negative charged molecular species – such as citrate), which are very important for applications [13–16, 31, 32, 45, 48]. Computer simulation was employed to understand the HAP NPs structural, electrical (dipole momentum and polarization – surface charges) properties by molecular mechanics (MM+, BIO CHARM, OPLS, etc.) and by quantum-mechanical semi-empirical (in PM3 parametrization) in restricted and unrestricted Hartree-Fock approximation (RHF and UHF) and by Density Functional Theory (DFT) methods using HyperChem 7.5/8.0 (based on personal computer). For more precise HAP crystal structure studies we use and analyze recently developed DFT approaches on Linux-clusters, such as

local density approximation (LDA), using local basis in AIMPRO codes [6, 52, 56, 68] and generalized gradient approximation (GGA), using plane-wave in VASP codes [7]. Particularly, HAP optical properties based on the computed by these DFT methods data of electronic Density of States (DOS) and electronic work functions obtained, are described and analysed. Beyond HAP crystal bulk model, a special HAP model of the layered slab super-cells units, which includes vacuum spaces between the layered slabs forming HAP surface, are considered and analysed too [5]. More computational details are described in [22, 24, 26, 27, 30–35, 67] and in sections below.

1. HAP CLUSTERS AND NANOPARTICLES

1.1. Formation of HAP crystal from HAP NPs in various conditions, size and shape effects

Investigations of the HAP crystal growth processes in various conditions show that the main growth units of HAP crystals are the initial clusters and that growth proceeds through the accumulation of these clusters, with diameter of about ~ 1 nm [41]. Naturally, HAP is a mineral form of calcium apatite with the formula $Ca_5(PO_4)_3(OH)$, but it is often written as $Ca_{10}(PO_4)_6(OH)_2$ to denote that the crystal unit cell comprises two molecular units. The specific feature of HAP is that the OH^- ions form inner channels along the *c* axis with various random OH-dipoles orientations under different external conditions, which allow the transfer of protons along this axis under special conditions (such as temperature heating and applied electric field with necessary critical values) [28–32, 35]. Usually HAP has 2 main different forms of nano-crystalline structures (in hexagonal $P6_{3/m}$ and monoclinic $P2_{1/b}$ space group structures) and amorphous structure. But depending on OH-dipoles orientations it has also two order variations: hexagonal disordered $P6_{3/m}$ with spatially random distribution of OH-dipoles over the whole of the crystal between the neighboring unit cells, and ordered $P6_3$ with parallel orientation of ones. The same is valid for monoclinic phase having disordered $P2_{1/b}$ group with oppositely oriented OH-dipoles in neighboring OH-columns and ordered $P2_1$ group with parallel OH-dipoles. Various HAP structures were determined experimentally by X-ray diffraction method and all the experimental data obtained are stored in special crystallographic databases, such as [4]. Some examples of these data are presented in Table 1 and corresponding image of HAP hexagonal unit cell consisting from 44 atoms is shown in Fig. 1, the inner OH-channels are shown in Fig. 2. For monoclinic phase consisting from 88 atoms it differs from hexagonal one by doubling of the unit cell along the *b* axis as shown in Fig. 3,a and Fig. 3,b. Fig. 3,c shows different orientations of OH groups dipoles. Both the phases are periodically repeated in space and form an ideal crystallographic structure for the whole of the crystal with exact positions for each atom. It is important to note that for such ideal crystallographic structures the relation of atoms Ca and P must correspond strictly to the correct stoichiometry, with a ratio of Ca/P of 1.67 [1, 5, 35]. In a real mineral there could be many deviations from such ideal structures, including such defects as various vacancies, interstitials and replacements of several atoms [32, 35]. Computational study allows us to construct similar ideal and defective HAP structures, though depending on the computational methods used. The finally obtained optimized positions of each atom and the parameters of the crystal unit cell could be slightly different and have variations. The main validation in this case is to test the computed results for various physical properties, corresponding to these structures, with experimentally observed data.

Table 1. Hydroxyapatite unit cell parameters *a, b, c* [Å] [4]

Phase	Group	*a*, Å	*b*, Å	*c*, Å
Hexagonal	$P6_{3/m}$	9.417	9.417	6.875
Monoclinic	$P2_{1/b}$	9.48	18.96	6.83

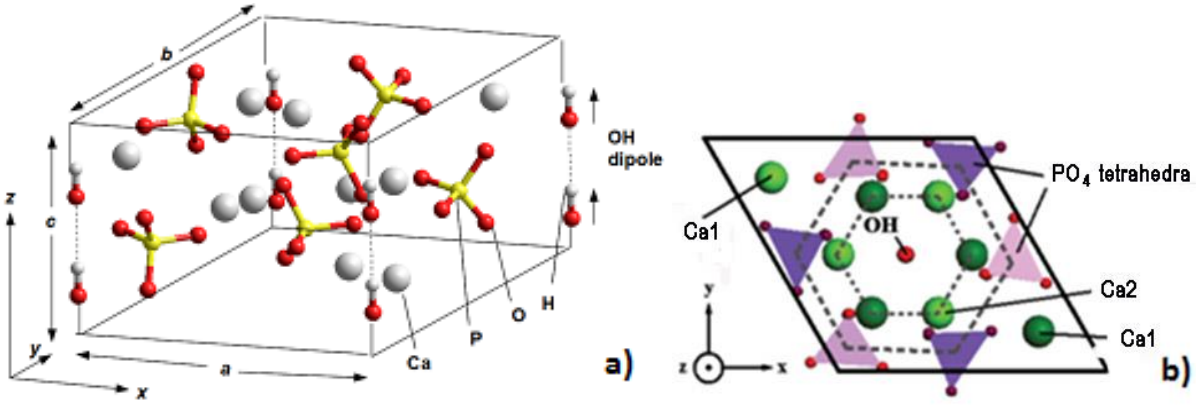

Fig. 1. Hexagonal HAP unit cell ordered structure. All OH groups are oriented in the same direction. They are positioned at the four corners of this unit cell, only one pair belongs to this unit cell, the other three pairs belonging to neighboring unit cells (i.e. one OH per unit cell): a) 3D-view of bulk hexagonal unit cell (printed with permission from IOP Publishing, LTD Copyright Clearance Center [35]), b) top view of hexagonal primitive cell (printed with permission from American Physical Society Copyright Clearance Center [22]).

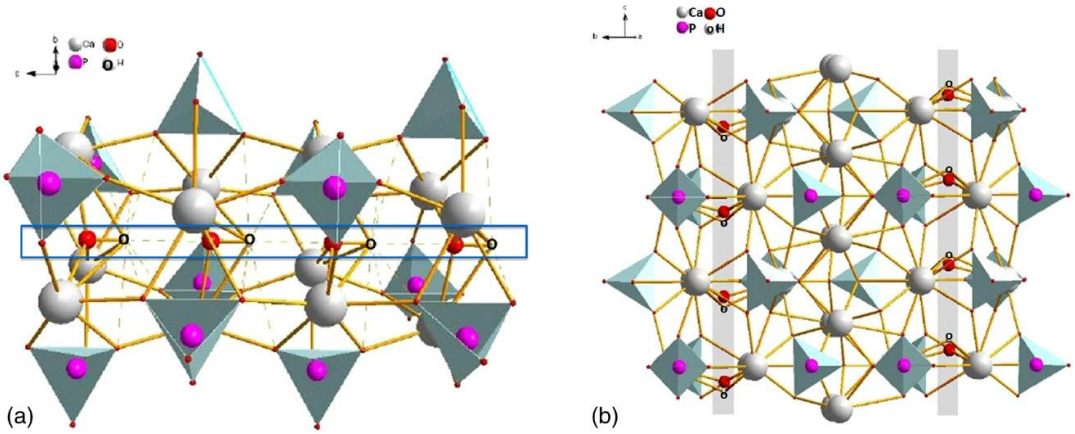

Fig. 2. Columnar OH-channel structures of HAP with different orientations: (*a*) OH-channel in ordered hexagonal phase $P6_{3/m}$; (*b*) OH-channel in monoclinic disordered phase $P2_{1/b}$ (each OH-channel is distanced *b*/2 from the next, and is oppositely oriented).(Printed with permission from IOP Publishing, LTD Copyright Clearance Center [30]).

Beyond the initial hexagonal configuration with all OH dipoles oriented in one “up” direction (init “0”), we also considered configurations with different OH orientations, such as: the opposite OH-dipoles oriented along the OH-channel outside the unit cell (oppo 11); OH-dipoles facing each other directed along the OH-channel inside the unit cell (oppo 22); all OH dipoles directed “down” (par 3), in opposition to the initial “up” configuration. These orientations are all shown in Fig. 3,c. The finally calculated optimized data for HAP (Table 5, below) show variations of the unit cell total energy with these different orientations of OH groups.

The amorphous calcium phosphate (ACP or a-HAP) phase is in the form of spherical grains of diameter ~ 300–1000 Å, while the HAP crystal forms needle-like crystal´s structure [1, 42]. An X-ray radial distribution study demonstrated that the a-HAP contains definite local atomic order and micro-crystalline (or ordered domains) about ~ 8.0–9.5 Å in extent rather than a random network structure [42]. For further study we can consider here several main clusters revealed from HAP structures in various cases.

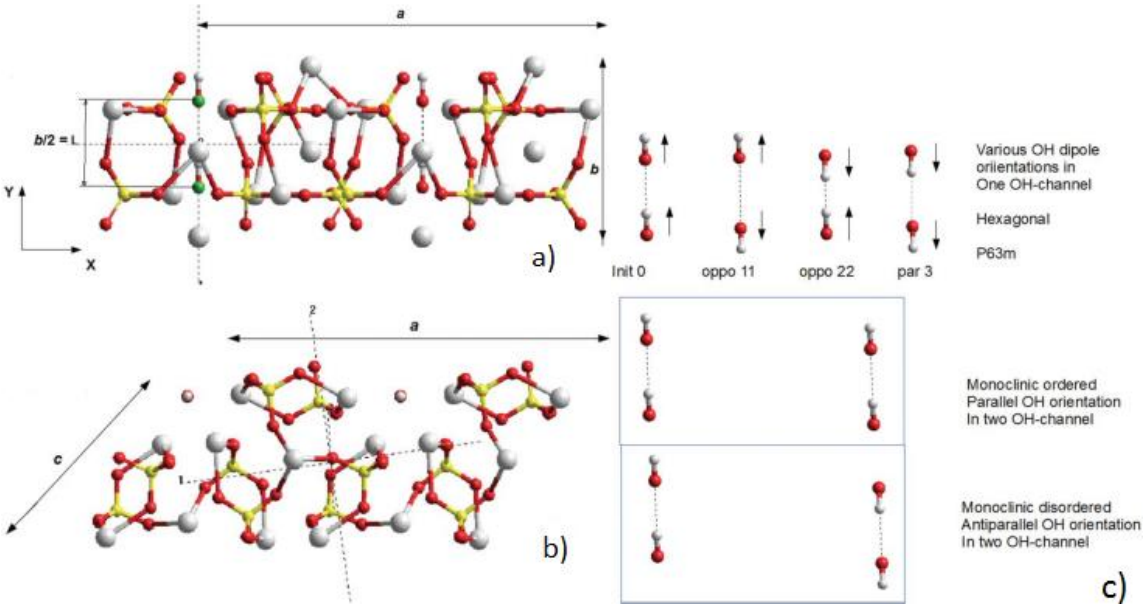

Fig. 3. Molecular model of the monoclinic ordered HAP: a) view along *b* axis, b) upper view. Initial optimized unit cell parameters: a = 18.980 Å ~ 2c, b = 6.9893 Å, c = 9.4801 Å. Space group $P2_{1/b}$ (printed with permission from Taylor & Francis Copyright Clearance Center[43]). c) Scheme of the main orientations of OH groups (printed with permission from IOP Publishing, LTD Copyright Clearance Center [35]).

Fig. 4,a shows the unit cells of apatite crystal structures projected on the *ab*-plane from Onuma work [41]. Given that the size of these clusters is 0.8–1.0 nm and that their composition has a Ca/P ratio of 1–8, the circled region is the part of the structure most likely to be a cluster. If it is, in this case it is a $Ca_9(PO_4)_6$ cluster measuring 0.815 nm along the *a*-axis and 0.87 nm along the c-axis. This cluster forms close hexagonal packing in the *ab*-plane; the gaps between clusters can be assumed to incorporate the remaining calcium ions and hydroxyl ions, thereby forming a HAP structure. In this model, since an apatite framework can form solely from the combination and stacking of clusters, there is no need for the remaining calcium ions to be incorporated into the crystals in the same way as the clusters. This provides a very convenient explanation for the "maturation phenomenon" in which the Ca/P ratio of apatite gradually increases towards the stoichiometric ratio of 1.67 after the crystal has been deposited. A particularly interesting aspect of this cluster accumulation model is that the stacking of clusters occurs along the *c*-axis.

Frequently considered Posner's cluster (PC) as it appears in crystalline HAP has C3 symmetry [42], $Ca_9(PO_4)_6$, Fig. 4,c, Fig. 5 and Fig. 6,c, when it is extracted without relaxation from HAP (Fig. 6,c). It has a layered structure, with each of two parallel layers containing three PO_4 groups, and three Ca's, where each triad forms an equilateral triangle. Posner's cluster in vacuum has lost the atoms that surround it in HAP, which must result in a number of unsaturated bonds including dangling bonds. This will inevitably lead to atomic rearrangement in order to improve the local atomic environment and increase the stability, which will lower the symmetry below that in HAP. Hence, it was supposed that formation of such PC cluster $Ca_{9(}PO_4)_6$, can play role also in the plastic deformation of HAP both in crystal and in a-HAP, due to "slippage" in the inter-cluster boundaries, characterized by a lower bond in comparison with intra-atomic bonds.

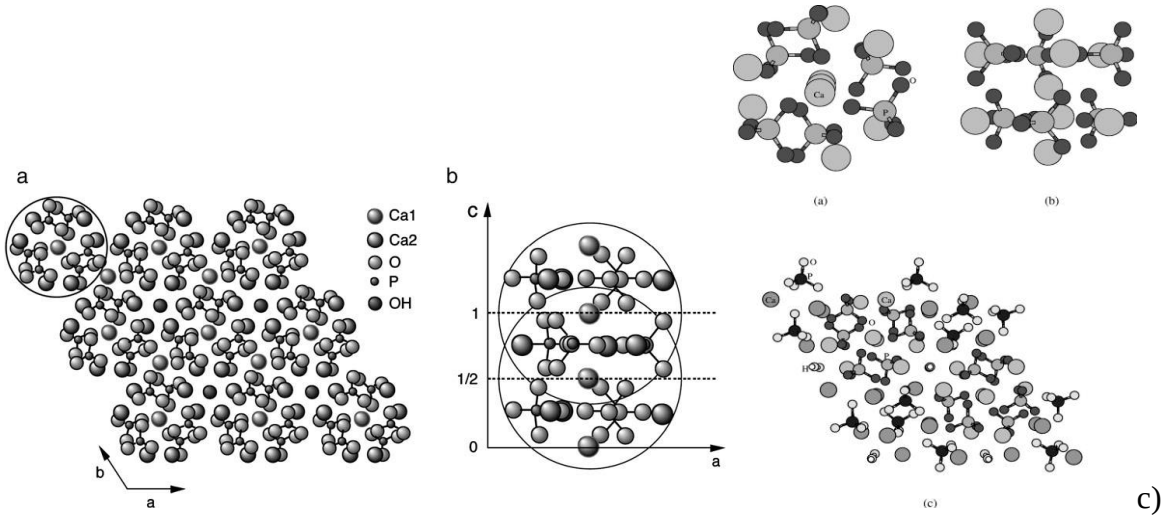

Fig. 4. Schemes of various structures for HAP cluster models: a) HAP structure projected on *ab*-plane; b) HAP structure projected on *ac*-plane (chiral clusters are defined) from [41]; c) Posner's cluster (printed with permission from AIP Publishing, LLC and Copyright Clearance Center [42]).

The authors of [30] picked out another cluster (HAP 3-411), which is shown in Fig 5,a and Fig. 6,d, and undertook the study of various sizes and shapes of HAP NPs formation under different conditions, particularly with variation of protons or pH of the medium. The main peculiarity of this cluster is that it has inside the central *OZ*-axis along *c* unit cell axis, which coincides with the direction of OH-column and orientation of OH-dipoles (Fig. 2). This cluster has a HAP unit cell shifted to the center of OH-column, which has partly omitted Ca atoms usually described as Ca1 (Fig. 1,b) and kept only Ca2 atoms in the central part around OH-channel. One of the main results obtained by this approach is that the interaction and aggregation of HAP NPs must depend on the concentration of bonded hydrogen atoms (protons).

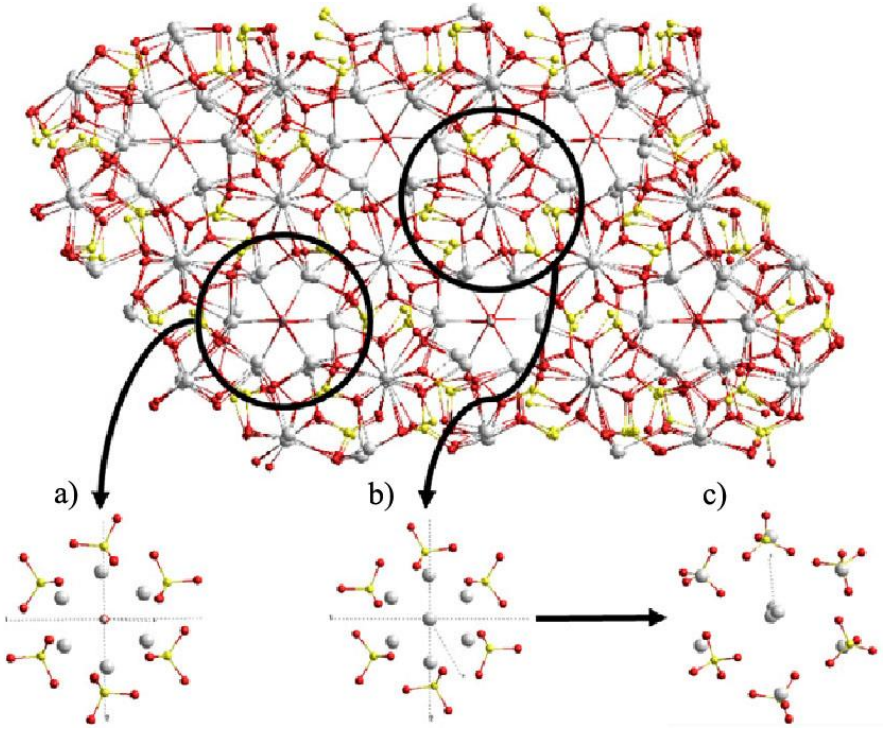

Fig. 5. Scheme of cut-off presentation for minimal HAP clusters: a) minimal HAP cluster (HAP 3–411) with only one OH channel and a minimal of inter-layers between Ca atoms (only two layers); b) PC in C3 symmetry PC(C3); c) relaxed PC with C1 symmetry (printed with permission from IOP Publishing, LTD Copyright Clearance Center [30]).

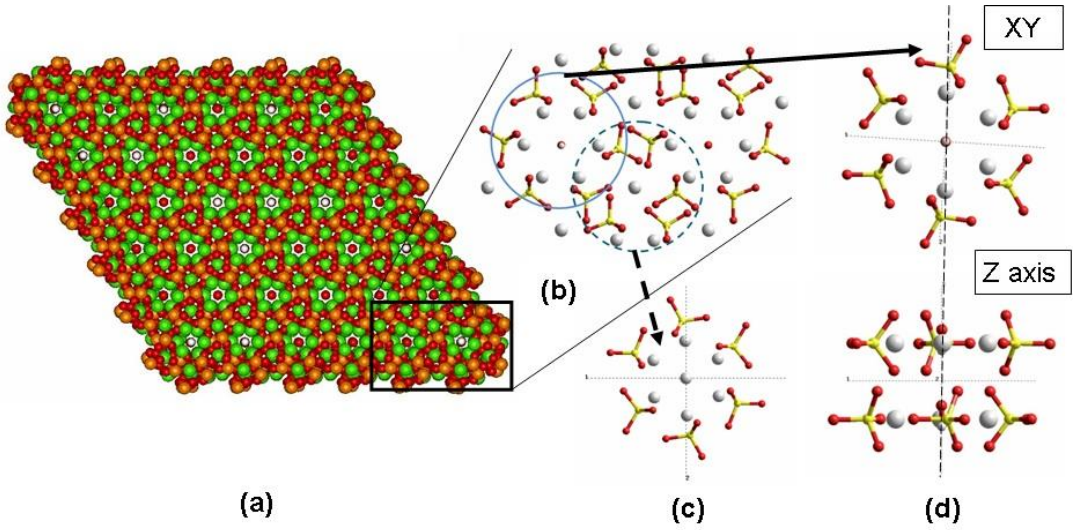

Fig. 6. Clusters of HAP extracted from the hexagonal HAP crystal model with 36 OH-channels: a) top view of big HAP cluster with 36 OH-channels; b) scheme of various minimal clusters extraction; c) Posner's cluster (PC); d) minimal cluster with 1 OH-channel, named as HAP 3–411 (modified and printed with permission from IOP Publishing, LTD Copyright Clearance Center [30]).

To test this point the authors performed a series of calculations of the HAP NPs interaction depending on the distances between NPs for two types of clusters – without any added hydrogen and with it. The hydrogen atoms subsequently filled the broken hydrogen bonds, up to six hydrogen atoms may be added in the case of totally filled hydrogen bonds for the small HAP cluster. These cases are shown in Fig. 7,a–c.

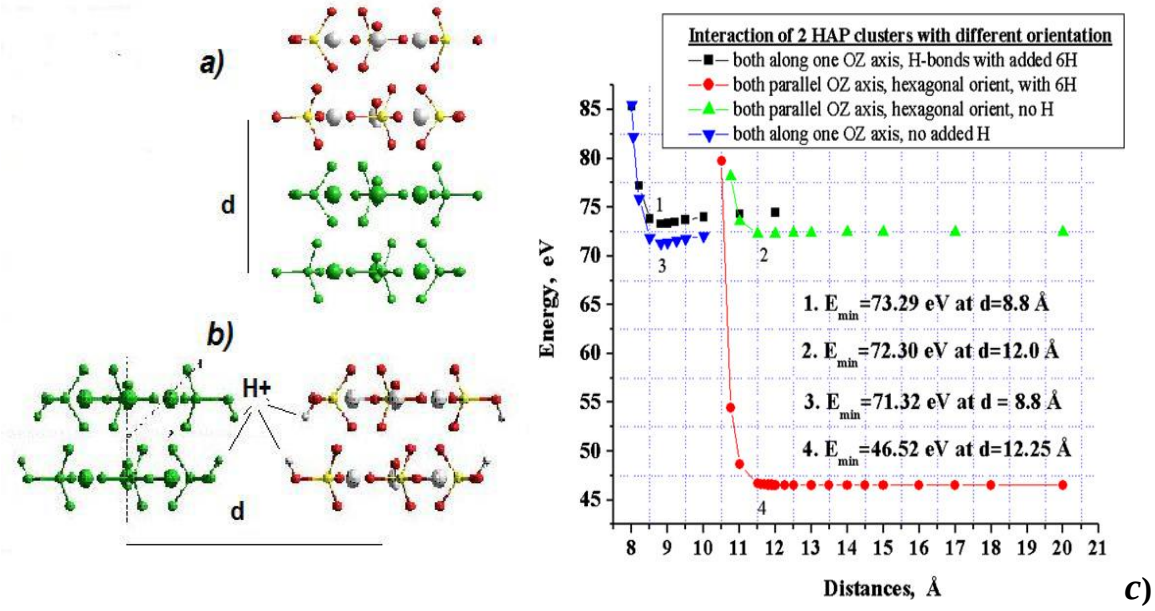

Fig. 7. Interaction energy of two HAP NP clusters against distances between them for two different orientations and various proton saturations of hydrogen bonds. Right figures present the interaction of two HAP NP clusters: a) with clusters orientation along the *OZ*-axis and b) with clusters orientation parallel to the *OZ*-axis; c) changes of energies with distances between HAP NPs. The green color in the above figures shows the selection option computed by the HyperChem molecular structure in the self-consistent field of another structure (printed with permission from IOP Publishing, LTD Copyright Clearance Center [30]).

The result of such modeling is shown in Fig. 7,c (the modeled and interacting molecular structures are presented in Fig. 7,a and Fig. 7,b) the minimal interaction energy corresponds to the case with six added hydrogen atoms and parallel orientation of the interacting NPs. For the case without hydrogen the minimum energy $E_{\min}$ is for orientation of both NPs along the same *OZ*-axis (relative values of condensation energies E_{cond} and optimal distances R_{opt} for these interactions are presented in Table 2).

Table 2. The interactions between the two orientation types of the HAP NP structures (printed with permission from IOP Publishing, LTD Copyright Clearance Center [30], Suppl. Mater.)

Type of inter-NP structure	Energy of inter-NP condensation E_{cond} without H (high pH)		R_{opt} of inter-NP at $E_{\min}$	$E_{\min}$	Energy of inter-NP condensation E_{cond} with full added H, (low pH)		R_{opt} of inter-NP at $E_{\min}$	$E_{\min}$
	kcal/mol	eV	Å	eV	kcal/mol	eV	Å	eV
Parallel	4.843	0.21	12.00	72.30	0.231	0.01	12.25	46.52
Along *OZ*	17.987	0.78	8.80	71.32	27.673	1.20	8.8	73.29

These data are close to proton transfer data for minimal distances and energy 0.78 eV along OH-channel in HAP [13, 14, 30], the condensation energy corresponds to the known data on the HAP [44].

The results obtained confirm and clarify the mechanism of the earlier discovered size effect of HAP NPs, which is related to the electrical properties of HAP NPs (dipole moment, polarization, surface potential and electron work function) [37–40, 48]. Second, the interaction of HAP NPs and the resultant shapes of their growth and aggregation directly depend on the concentration of hydrogen atoms (or protons) in the surrounding media, which usually determines pH. These results lead to the following conclusions:

– when the pH is high (low protons) the HAP NPs interact and formation of needle-like tubes or columnar structures oriented preferably along the *OZ*-axis occurs;

– when the pH is low (high protons) the HAP NPs interact perpendicularly to the *OZ*-axis direction to form conglomerates in hexagonal orientation and sphere-like or bundle-like shapes.

These results are corroborated by several experimental studies of the nucleation and growth mechanisms of HAP NPs in the presence of various compositions of the solution, such as citrate species [45] or nonionic surfactants [46]. These results correlate with recent HAP studies, showing that the basic inorganic building blocks of bones and teeth are nanocrystalline and NPs combined into self-assembly structures under the control of bioorganic matrices [17]. The data obtained could provide background for studies of the intrinsic formation of various shapes of HAP following precipitation from various aqueous solutions [30] and in-body solutions.

1.2. Main features of electrical field, charges and potential inside and outside the HAP surface

Other important results of [30] are that changes in dipole moments, polarizations and electrical field, as well as forbidden zone energy and work function changes were computed. First, it is worth noting that the emerging dipole moment's orientation, apart from its components D_x, D_y, D_z, has a certain variation. Second, it is seen that the component D_y, especially in the presence of saturated dangling hydrogen bonds with additional hydrogen atoms H (protons), has a strongly pronounced orientation to the plane *XOY* – namely at right angles to the axis *OZ* (Fig. 8), and rise of total dipole moment *D* with cluster sizes (Table 3).

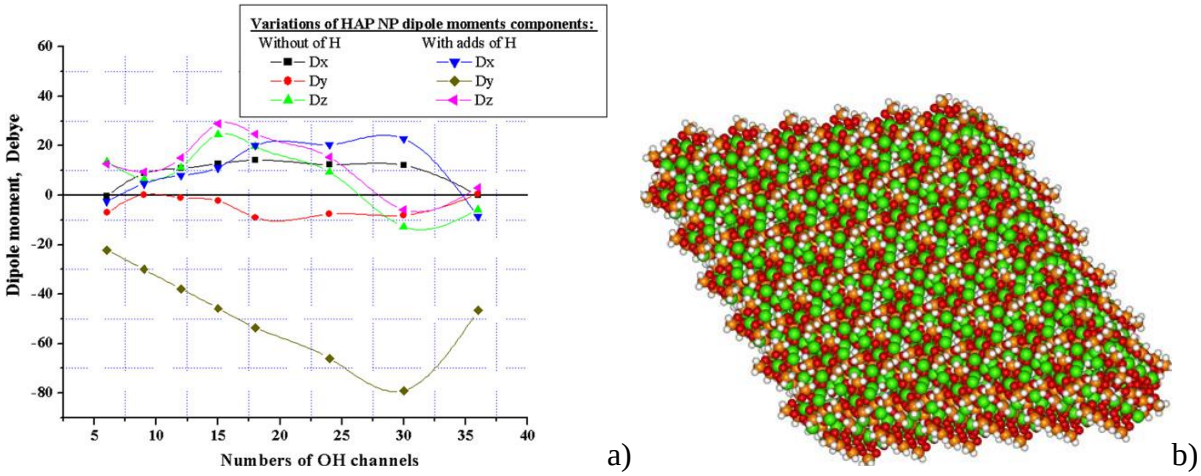

Fig. 8. Variations of different dipole moment components: a) HAP NPs with size (number of OH channels) and b) under the influence of added hydrogen atoms H (protons) filling all broken hydrogen bonds (printed with permission from IOP Publishing, LTD Copyright Clearance Center [30]).

Table 3. Change of dipole moment of HAP NPs with cluster size for different types of Hydrogen Bonds (printed with permission from IOP Publishing, LTD Copyright Clearance Center [30], Suppl. Mater.)

Number of cluster OH channels	Unsaturated hydrogen bonds			Saturated hydrogen bonds		
	Volume *V* (VdW), nm^3	Dipole moment, *D*	Polarization *P*, *10^{-3} C/m^2	Volume *V* (VdW), nm^3	Dipole moment, *D*	Polarization *P*, *10^{-3} C/m^2
2	4.58	6.56	4.781	5.029	10.85	7.107
3	7.03	11.48	5.445	7.719	21.14	9.137
6	11.50	15.36	4.456	12.60	25.60	6.78
9	19.24	10.96	1.901	20.82	31.72	5.08
12	24.44	15.56	2.124	26.44	41.55	5.24
15	29.66	27.79	3.126	32.08	55.30	5.75
18	34.87	25.93	2.480	37.76	62.37	5.51
24	43.58	17.32	1.326	47.21	70.80	5.00
30	52.81	19.32	1.221	57.10	82.45	4.81
36	64.44	5.83	0.302	70.25	47.42	2.25

Detailed calculations of structural, electrical and electron energies of these clusters show the following main important results [30]:

– the electron energy band structures of initial HAP clusters computed by PM3 methods correspond well to the data reported (both experimental and simulated) [10, 21, 22, 26, 41, 42, 47] (see more details in [30] and in Table 4) – the main values obtained for the energy gap are $E_g \sim 3.54$ eV for fixed PC (C3 symmetry), $E_g \sim 4.56$ eV for relaxed PC (C1 symmetry) as compared with known data $E_g \sim 4.43$ eV for the last structure in [41, 42], and $E_g \sim 5.41$ eV for the smallest HAP (C1 symmetry) as compared with $E_g \sim 5.38$ eV for fixed HAP bulk [42];

– the computed data show some variations of the energies of the electronic band structures (*E* HOMO and *E* LUMO) with the addition of hydrogen atoms and corresponding variations of E_g (4.02–5.56 eV, see Table 4), and have a tendency for a decrease of E_g at the finally filled hydrogen bonds – all these data are in good agreement with the experimentally measured $E_g \sim 4.0$ eV for a surface charged HAP samples in [47];

– the change of the total dipole moment and polarization are varied with increase of added hydrogen, but average values slightly decrease as compared with the initial state (see Table 3, Table 4).

These results are very urgent for practical applications, because recent studies of the influence of electrical charge on HAP specimens surface on the osteoblast behavior and bone tissue growth clearly show that the deposition on the HAP surface of a negative charge enhances attachment and proliferation of the osteoblasts and fabrication of the bone tissue [36–40].

Moreover, it was established that the hydrogenation [15] of the HAP specimens increases their surface electron work function. This means that the surface electrical charge becomes more negative in contrast with the native specimens. The shift of the charge to the negative value leads to the enhanced proliferation of the cells. Let us see, how it is connected with the models considered.

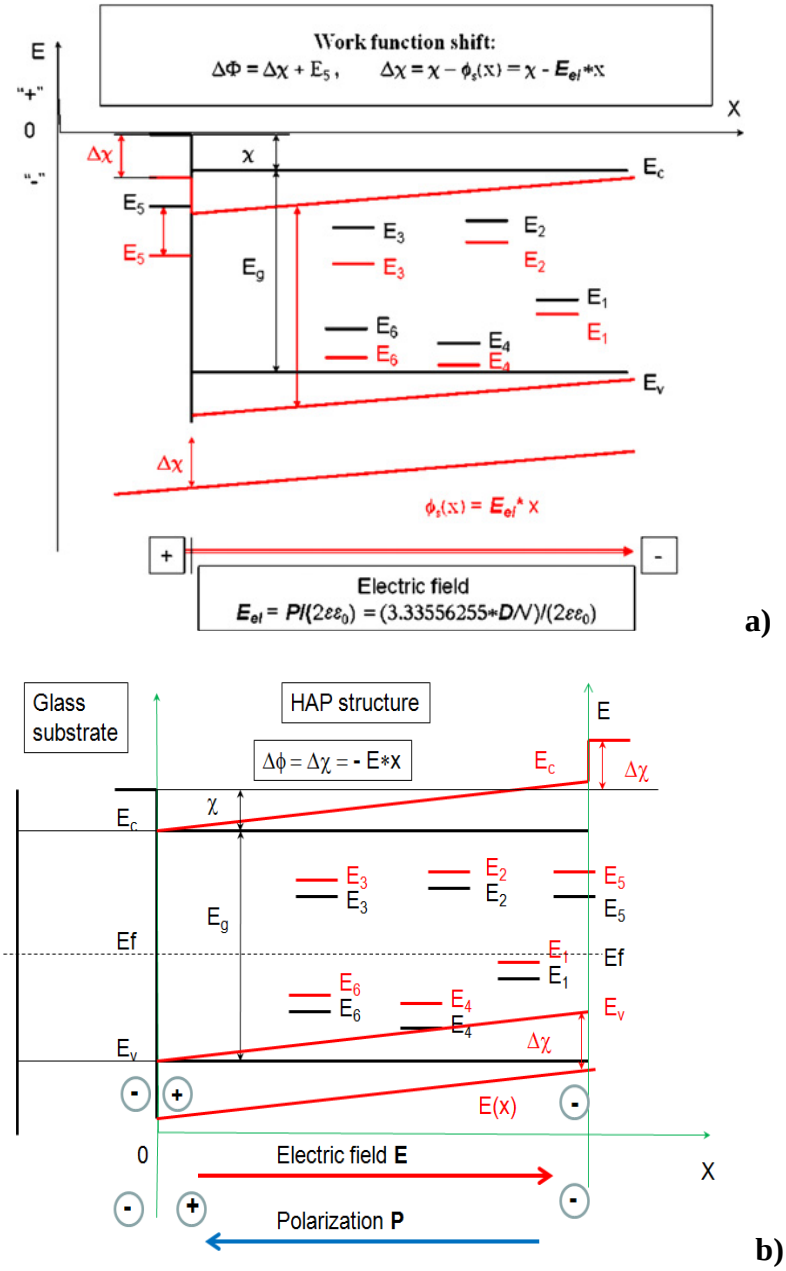

Fig. 9. Scheme of HAP NP energy band structure and its shift by the internal electric field E_{el} arising, due to the polarization P of the HAP cluster: a) in vacuum, b) on negative substrate (partly modified and printed with permission from IOP Publishing, LTD Copyright Clearance Center [30]).

Table 4. Minimal HAP cluster HAP 3–411 with variation of added protons (hydrogen atoms) computed by PM3 method in UHF approximation, with corresponding volume variation on the Van der Waals surface from V(0H) = 0.346 nm^3 up to V(6H) = 0.361 nm^3 (printed with permission from IOP Publishing, LTD Copyright Clearance Center [30], Suppl. Mater.)

HAP cluster (+added H)	E_g, min value, eV	Polarization total, C/m^2	Dipole moment, Debye	Change of E_{total}, eV
HAP + 0H	5.408799	0.112060	11.614	0.00000
HAP + 1H	4.025690	0.181090	18.909	–13.073
HAP + 2H	5.438408	0.041797	4.397	–26.146
HAP + 3H	4.990902	0.112138	11.885	–39.219
HAP + 4H	4.529548	0.103650	11.066	–52.2934
HAP + 5H	5.564552	0.045649	4.909	–65.366
HAP + 6H	4.632705	0.101396	10.983	–78.4397

It is necessary to note that the polarization values calculated in this model are not so large (the most important data is at the level ~ 0.5 μC/cm^2 that is less than the known data for HAP polarized by an applied electric field [12]), but this polarization is essential for this HAP NP structure, because it appears and exists as spontaneous (self-induced or self-organized) polarization similar to the ordered dipole momentum as in ferroelectrics (see also in [43]). This polarization – as revealed by the surface charges on HAP NPs – leads to the existence of an electric field inside the cluster. This internal electric field must shift the entire energy band structure of the HAP NPs; the largest shift evidently influences the surface energy levels. In this model the shift of the surface level energy under the influence of the internal electric field depends on the NP size and consequently on the corresponding change of the electron work function for NPs with size variation (as estimated in [30, 37–39, 48]).

Because HAP is preferably an insulator (or p-type semiconductor [47] with wide forbidden energy gap E_g > ~ 4 eV), it have as usual dielectric a rather large screening Debye length L_D. Therefore, the dependence of the displacement of the energy bands looks linear for the considered HAP clusters. There is an experimentally established [47] surface level with the energy $E_5 = E_v + 3.3$ eV, giving a major contribution to the photoelectric effect (see on Fig. 9, here the E_i energies are the bulk energy levels, χ is the electron affinity, ϕ is the electron work function). It is natural to assume that the photo-excitation happens from the surface level. Therefore, this level gives the maximum shift in the electric field polarization proportionally to the linear size of the cluster. So, from this model we can estimate that the shift of the surface level energy under the influence of the internal electric field depends on the NP size, the corresponding change of the electron affinity Δχ and the electron work function ϕ for NPs with size variation (Fig. 9,a). The average value of polarization has been evaluated as $P \sim (5–5.2) \times 10^{-3}$ C/m^2 (see data from Table 3). The surface charge $\sigma = P$ creates the electric field $E_{el} = \sigma/(2\varepsilon\varepsilon_0) = P/(2\varepsilon\varepsilon_0) \sim (0.28–0.295) \times 10^9$ V/m, for ε = 1, where ε is the relative dielectric permittivity of the media, and $\varepsilon_0 = \varepsilon_0 \approx 8.85 \times 10^{-12}$ F/m. For our estimation we took the average value of ε = 10 (are several reports in HAP on ε from 5 up 15 [7, 10, 30, 44]). In this case an electrical field exists inside the HAP NP must be: $E_{el} \sim (0.28 – 0.30) \times 10^8$ V/m, appearing as a result of surface charges, which can shift all the NP energy levels, including the surface level and work function, and this shift must depended on the NP size values. For HAP NPs with the size $x \sim 5$ nm this shift of energy on the NPs' surface $\Delta E = E_{el} \times x \sim 0.14–0.15$ eV. For the experimental data for HAP NPs [30, 35, 48] with size variations between two NPs of ~ 20–60 nm and sizes of more than ~ 100 nm, the average differences in the effective radii of these two compared NP classes could be estimated as $\Delta x \sim 10–20$ nm. So, in this case, the change of the surface energy level and corresponding work function shift must be estimated as:

$$\Delta\phi = \Delta E = E \times \Delta x \sim (0.28–0.30) \times 10^8 \text{ V/m} \times (10–20) \times 10^{-9} \text{ m} \sim 0.28–0.60 \text{ eV}.$$

This value is close to the shift of the electron work function ϕ_{exp} = 0.3 eV directly measured by photoelectron spectroscopy. A derivation of the emission current for a photon energy demonstrated a sharp maximum at 5.2 eV for sizes in the range ≈ 20–60 nm, while NPs with a size range > ~ 100 nm indicated the maximum at 5.5 eV [30, 35, 48] (Fig. 10,a). The developed model is simplified for the rough estimation, but we believe that it demonstrates the essential features of this phenomenon, in principle. The magnitudes of the experimentally measured work function were directly proportional to the typical sizes of NPs (Fig. 10,b) [30, 48], which are in accordance with the above simulation results in respect of *P* values, when the cluster size is larger.

Here, we must note, that if electrons excite from positive charged side of HAP sample (Fig. 9), [30, 48], here must be decreasing of the work function, because in this case electrons have most easy way through sample surface. However, if we carefully look on the sample preparation for these experiments, we found that during this preparation HAP NPs have following treatment [30, 48]: all HAP NPs were composed as the nanopowders, which were mixed with ethanol to reach a cream-like emulsion; then it was deposited on glass wafer and dried during 1 hour at room temperature and atmosphere. After that the specimens were placed in photoelectron emission spectrometer for measurements.

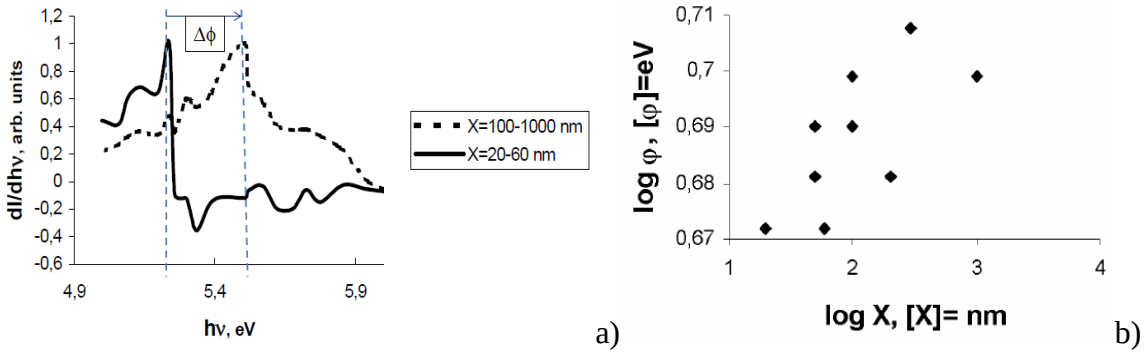

Fig. 10. Experimentally registered shift of work function with HAP sizes: a) intensity changes; b) work function changes (printed with permission from IOP Publishing, LTD Copyright Clearance Center [30], Suppl. Mater).

But, as we know from our another work [49], where was made the special test for glass substrate in similar condition with polymer specimens having the polarization, the glass substrate have own surface negative charges, which particularly increased during ultraviolet irradiation in the same photoelectron spectrometer. Therefore, the HAP NPs could be reoriented on such negatively charged glass surface to positioning with its positive side on the glass substrate and with negative side outside to upper surface from which electrons can escape from samples (Fig. 9,b). In this case we must consider other true schematics of energy bands shift with correct rising of electron work function. So, it is relative effect and it has principal nature.

2. BULK HAP CRYSTAL STRUCTURES

2.1. Infinite periodical lattice and electrical potential

In this section the results of modeling and calculations based on the initial HAP hexagonal unit cell model (see Section 1.1, Fig. 1, Table 1) are described. This description is presented in the framework of the density functional theory (DFT) approach in the local density approximation (LDA) using AIMPRO code [52–54] in combination with HyperChem modeling [55, 56]. The computational details and all the data obtained recently are presented in paper [35]. For initial calculations, the experimental data were taken from [4], which were highly confirmed. Using these data the initial hexagonal HAP unit cell structure and

optimized ones were calculated through AIMPRO code with various values of Monkhorst–Pack *k*-point meshes and cutoff for kinetic energy. The best result for cutoff at the level equal to 300 a.u. and the standard Monkhorst–Pack *k*-point meshes 2 × 2 × 4 were obtained and used in all the calculations [35].

As it was shown in [32, 35] for these calculations, necessary precision is attained for the valence configuration of the Ca atom model with 2 electrons – ($4s^2$) shell. The calculated equilibrium HAP unit cell parameters were $a = b = 9.4732$ Å and $c = 6.9989$ Å for pure hexagonal $P6_{3/m}$ phase, and $a = 18.950$ Å, $b = 6.997$ Å, $c = 9.474$ Å for pure monoclinic $P2_{1/b}$ phase. This result is comparable fairly well with the experimental data [4] and the data computed in [35]. One of the main results is that it has the minimal total energy for hexagonal HAP structure after optimization at the level of –467.09923 a.u. per a unit cell. The data of all atomic positions for this optimized initial pure HAP hexagonal unit cell, consisting from 44 atoms, are presented in Table 1S in Supplementary materials of the paper [35]. To study the unit cell ground states in greater detail, the unit cell total energy with different orientations of OH groups was calculated (Fig. 3,c). The calculated data for HAP (Table 5) show variations of the unit cell total energy with these different orientations of OH groups. Similarly, two main different orientations of OH groups for the monoclinic HAP phase, with parallel and antiparallel orientations, were also considered.

One of the main peculiarities of the results is that the computed data clearly show that the HAP monoclinic phase (with oppositely oriented OH^- ions in the neighboring channels) has lower energy as compared to the HAP hexagonal phase, which is ~ 24 meV (Table 5). These results are comparable with the data obtained by other authors [10, 21] and are very close to the data from [22]. Comparison of the calculated value of the forbidden energy band E_g ~ 4.6 eV [32, 33, 35], with other data computed show that all E_g data are very close to the data obtained in [35]: E_g ~ 5.4 eV from Calderin and Scott [9], E_g ~ 5.23 eV from Slepko and Demkov [22], E_g ~ 4.51 eV from Rulis et al [26]. Furthermore, the computed values of the forbidden energy gap E_g, are in good agreement with [9, 10, 20–22, 25, 27].

Table 5. HAP structural and physical properties, computed by AIMPRO (modified and printed with permission from IOP Publishing, LTD Copyright Clearance Center [35])

HAP type	Lattice Parameters, Å	E_g, eV (± 0.05 eV)	$\Delta E_1 = E(P2_1) - E(P6_3)$, meV/cell	$\Delta E_2 = E(P2_{1/b}) - E(P6_3)$, meV/cell	$\Delta E_3 = E(P6_{3/m}) - E(P6_3)$, meV/cell
Hexagonal 0 $P6_3$	$a = 9.4732$ $c = 6.9986$	4.60	–	–	–
Hexagonal 11 $P6_{3/m}$	$a = 9.4624$ $c = 7.0182$				+131.98
Hexagonal 22 $P6_3$	$a = 9.4580$ $c = 7.0225$				+130.62
Hexagonal 3 $P6_{3/m}$	$a = 9.4754$ $c = 6.9964$				+1.905
Monoclinic $P2_1$ (OH parallel)	$a = 18.980$ $/2 = 9.4898$ $b = 6.9893$ $c = 9.4801$	4.56	+1.63 meV	–	
Monoclinic $P2_{1/b}$ (OH opposed)	$a = 18.950$ $/2 = 9.4897$ $b = 6.9971$ $c = 9.4740$	4.68	–	–24.22 meV	

The calculated data of the ordered $P2_1$ form (with oriented in parallel OH^- ions in channels) exceed the value of the hexagonal $P6_3$ form, by the value of ~ +1.63 meV. In both cases, differences in these values are not very large, and are within the limits of usual thermal energy at room temperature of < 25 meV. This is a very important result, as it means that all

these different phase structures of HAP can co-exist at room temperature, and HAP can easily transfer from one form to another, depending on the environmental conditions (and changes of the stoichiometry ratio). Possible mechanism for the phase transition between the hexagonal and monoclinic phases could be thermo-activated switching of OH-dipoles in HAP OH-channels and changes of the proton positions around [13, 14, 22]. This leads to the possibility for local fluctuations to arise between the phases in space leading to variations of the HAP surface profile due to occasional changes of the neighboring phase.

Evidence for this fact could be observed by atomic force microscopy (AFM), showing coexisting of the double-phase local regions at the nanoscale. It should also be emphasized that the monoclinic ordered phase, $P2_1$, could have piezoelectric features in this case [50, 51].

This problem has been analyzed recently in paper [43]. In this case the polarization per unit cell of the order of $P \sim 0.0038$ C/m^2 was obtained, due to parallel orientation of OH dipoles and this means that it is a ferroelectric phase. It is interesting that, this value is fully in line with the data obtained earlier from cluster models ($P \sim 0.005$ C/m^2) [30]. Corresponding piezoelectric coefficient for this case on the order of $d_{yy} = d_{33} \sim 15.7$ pC/N ~ 15.7 pm/V was estimated in [30], which is very close to value $d_{33} \sim 16$ pm/V measured in [50], and is twice larger than the value of the experimentally measured in [51] effective piezoelectric coefficient $d_{33eff} \sim 8$ pm/V, which varies significantly from grain to grain. This deviation was explained in [43] by polar properties variation for different grains: piezoelectric contrast (observed in Ref. [51]) is registered only in some polar grains (ordered monoclinic HAP) and is averaged with other non-polar grain contribution (disordered hexagonal HAP). The resultant contrast turns out to be nearly twice less than the calculated value (corresponding to the case when all the grains are polar).

Another important remark is that the performed DFT calculations of the electronic density of states (DOS) determine the top of the valence band E_v, bottom of conductive band E_c and corresponding value of the forbidden energy gap $E_g = E_c - E_v$, as well as allow us to study the influence of lattice charges changes on the shift and changes of the values for these E_v, E_c and forbidden zone E_g [32, 35]. These results are in principal agreement with experimental data on living cells attached to the charged HAP surface [36–40], and predict some new properties – the shift of the HAP electron work function ϕ changes in the HAP lattice charges, because the value of ϕ is directly connected with all these DOS parameters E_v, E_c and E_g (it will be considered below in greater detail). But it should be emphasized here, that it is changes in bulk unit cell of HAP, while, of course, more exact calculations will also need studies of the reasons for the HAP surface changes (deformations, atomic shifting, vacancies, etc.).

2.2. HAP crystal with defects (O, H, OH vacancies, H interstitials, substitutions)

Using computed data of HAP unit cell modeling by DFT LDA method it is possible to construct and calculate the models of several defects in HAP structure: O and OH vacancy, H interstitials, etc. For each optimized HAP unit cell structure the corresponding electronic density of occupied/unoccupied states (DOS) were calculated for a wide energy spectrum range. For studies of any defects in HAP in the work [35] the initial optimized hexagonal unit cell was used, in which the necessary structural changes were made (delete some of the atom or group, such as, O, H or OH, that create a vacancy, or insert additional atom, such as H, that create interstitials). Then, again the calculation of the optimal total energy for this changed HAP structure was performed, obtaining new positions for all atoms in the new optimized unit cell (Fig. 11). These calculations were made using AIMPRO code [32, 35, 52–54]. After that the DOS calculations was made for each optimized HAP structure. For each optimized HAP structure obtained here, the unit cell data were transformed into HyperChem format and models in HyperChem workspace with dipole moments calculated (by PM3 method, or similar) were constructed [55, 56]. In this case we can also obtain charges and electrostatic

field distribution in surrounding space, showing us the positions of the positive and negative charges and electric potentials lines in the space.

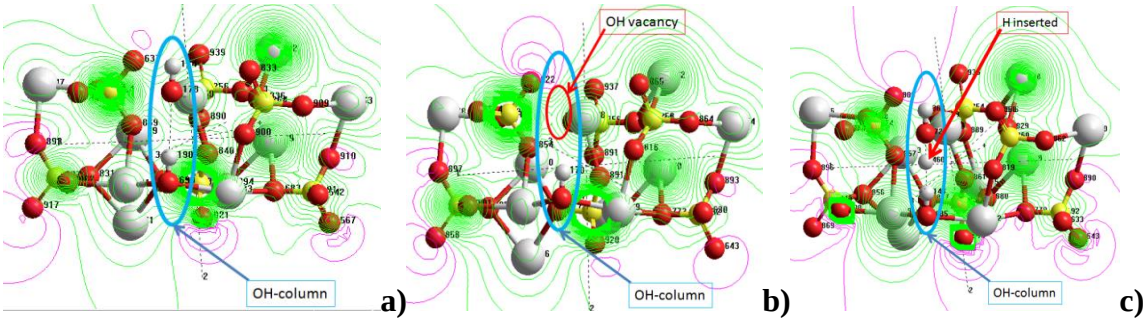

Fig. 11. Images of molecular structures for hexagonal HAP unite cell in HyperChem workspace: a) initial pure hexagonal HAP unit cell, b) HAP unit cell with OH vacancy in OH-columnar structure, c) HAP unit cell with H atom inserted in OH-columnar structure. Green lines – positive, red – negative.

Fig. 11 shows the optimized HAP unit cell structure and electrostatic potential distribution for initial pure hexagonal HAP (a) and examples of the HAP with some defects: OH vacancy (b) in OH column, and H interstitials (c) – as additional inserted proton in this OH column. As a result, one can see how the electrostatic field equip-potential lines change and the electrostatic potential is redistributed in the surrounding space. Calculation of DOS allows not only to determine the forbidden energy gap, $E_g = E_c - E_v$, but also shows the changes of the E_g value and the creation of the new additional energy levels, E_i, which arise inside the forbidden zone and correspond to the modeled defects of the unperfected HAP cell.

Let us consider the main scheme of the computed DOS structure (Fig. 12), which also presents possible connections with photoelectron emission experimental data. The upper right DOS image in Fig. 12 presents the DOS structure for the initial pure hexagonal HAP, and consists of several peaks (A, B, C and D) in the valence band, as well as several deep levels [35], which is in good agreement with the data obtained by other authors [10, 22–26] and corroborated by recent experimental data obtained by synchrotron technique [33, 34].

In this case, all the states and energy levels which are occupied by electrons are also marked by “green” color and the unoccupied energy levels and bands (such as in the conductive band) – by “red” color. When photoelectron excitation is applied to samples with sufficient energy (e.g., equal to or larger than the forbidden zone energy gap, $E_g = E_c - E_v$), electrons can be excited to the conductive zone. If additional energy is then applied, equal to or larger than the electron affinity χ, then electrons with a total energy $\phi = \chi + E_g$ can escape from the HAP sample, and be collected by detector. This border energy level is the electron work function ϕ, usually measured by the photoelectron emission (PEE) technique [33, 34].

For further analysis, here E_{g0} and ϕ_0 as the energy gap and work function for initial HAP were introduced, while for all the cases with defects, etc., the new changed values were E_g and ϕ. Supposing that electron affinity changes only slightly ($\chi \sim$ const $< \sim 1$ eV [47]), it is possible to compare the calculated data of all E_g changes under the influences of defects, etc., with changes of the electron work function, which were experimentally measured by PEE method. In this case, for all the changes it is possible to write that $\Delta\phi = \phi - \phi_0 = E_g - E_{g0} = \Delta E_g$. So, the calculated change ΔE_g corresponds approximately to measured $\Delta\phi$ corresponding to various defects, influences and obtained after any performed treatments.

However, this consideration is correct only for the case when any additional energy levels (E_i) are absent inside the forbidden zone E_g. If additional energy levels, or thin band, arise inside the E_g, electrons can be excited from these levels too, by photo-excitation, contributing to total electron flow and influencing $\Delta\phi$ changes. Such a situation is shown in the middle DOS image in Fig. 12,b, where a thin energy band E_i arises inside E_g. This energy level (or

thin band consisting from several close positioned levels) can also be occupied or unoccupied. The case under consideration is ½ occupied (as in the case of the OH vacancy, for example). It must be stated that an important factor for the experimental observation of such levels (bands), is that the susceptibility (or sensitivity) of the experimental system should be sufficient to detect the electron flow intensity.

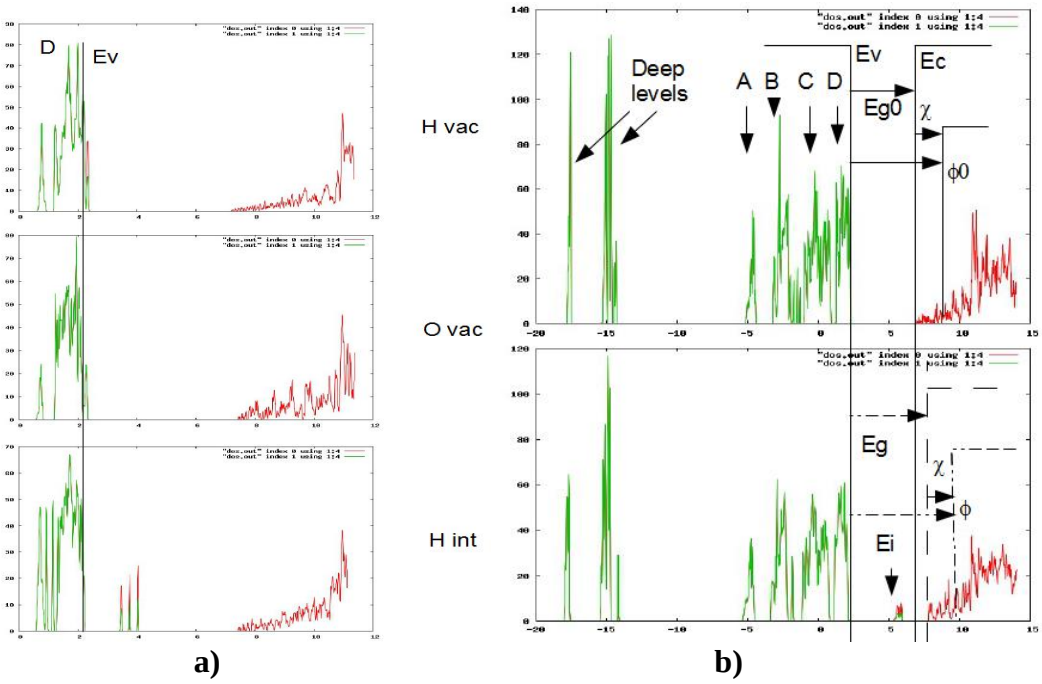

Fig. 12. Density of states (DOS) for HAP hexagonal structure: a) pure HAP and with OH vacancy (down); b) DOS of H and O vacancies (upper and middle), and H interstitial (bottom). Green shows energy levels occupied by electrons, red shows unoccupied energy levels. Horizontal arrows show the direction of the electron excitation, other arrows identify deep levels in valence bands of HAP (printed with permission from IOP Publishing, LTD Copyright Clearance Center [35]).

This means that the intensity of the excited electron flow from this E_i should be large enough in magnitude, and comparable with the intensity of some intensity peaks from the valence band, such as for peak D here (Fig. 12,a). In this case for OH vacancy, the intensities of these E_i peaks have maximum ratios to the first large peak from the valence band (peak D in Fig. 12,a) of ~ 5:60 ~ 0.08 for the HAP hexagonal unit cell (down image in Fig. 12,a). We must also note that these values correspond to rather high concentration of OH vacancies, because it corresponds to one OH vacancy per unit cell (which contains only two OH groups). Because the usual sensitivity of the intensity of PEE method is ~5 % (or ~ ratio of 0.05), if the ratio of intensity of the E_i peak inside E_i is less than this value, this PEE technique cannot accurately be used to observe such energy levels. Therefore, these results were really on the borderline of what could be experimentally observed by PEE, and may not be reliable.

2.3. DOS for O, H and OH vacancies and H and OH interstitials

The calculations of such important defects as H, O and OH vacancies, as well as H and OH interstitials were made in [35], by making the changes to hydroxyl OH groups using either atoms 43 and 44, or 28 and 29, for vacancies, and atoms 45 and 46 atoms for insertion of additional interstitials (for details see in Table 1S, in Supplementary Materials [35]). For vacancies, some data are already reported: for example, reference [27] gives values for oxygen and hydrogen vacancies of ~ 0.1 eV up from the top of the valence band, and for OH vacancies closer to the bottom of the conduction band. This is similar to data in [35], but more

detailed and exact values for vacancies were obtained here, and the data for interstitials were published for the first time here (see detailed data in Table 6 and Fig. 12,b).

As one can see, the energies obtained for O, H and OH vacancies are very close to the calculated data from [27]. The main result is that for O and H vacancies, the energy level created in the forbidden zone is very close to the top of the valence band (Fig. 12,b, upper and middle DOS image), while OH vacancies form a wider trapped band (or several closely positioned levels), placed approximately in the middle of the E_g, as shown on the lower DOS image in Fig. 12,a. Such regularity has been recently observed experimentally by using the synchrotron spectroscopy technique [33, 34].

These data are confirmed in reference [60], where it was observed that with heating of HAP samples (fabricated by the same PERCERAMICS [15] technology) the OH group is annealed and removed from the HAP surface, which leads to a rise in the energy level $E_i \sim E_v$+3.5 eV, which the authors of [47] connected with the rise of OH vacancies. As it can be seen, a similar value of energy for OH vacancies case was obtained in [35] (Table 6 and Fig. 12,b).

Therefore, OH vacancy influence is very important, because it leads to:

1) a high increase of E_g of ~ 0.86 eV; the shift from E_g ~ 4.6 eV for pure hexagonal HAP to E_g ~5.49 eV for HAP with an OH vacancy in one unit cell model.

2) creation of trapping levels (narrow bands) in the middle of the forbidden zone with energies of $E_i \sim E_v$ + (3.11–3.82) eV with peaks at 3.40, 3.53 and 3.66 eV, which serve as traps for electrons from the conductive band, and their recombination with holes.

Table 6. Characteristics of calculated defects in HAP structures, all optimized with the usual energy error ~ +/–0.05–0.1 eV for all DOS calculations (modified and printed with permission from IOP Publishing, LTD Copyright Clearance Center [35])

Defect type	Lattice parameters, Å	E_{gap}, E_g= $E_c - E_v$, eV	Change E_{gap} from init HAP, eV	E_i from E_v ($E_i - E_v$), eV	E_i from E_c ($E_c - E_i$), eV
HAP hex init $P6_3$	a = 9.4732 c = 6.9986	4.6	–	–	–
Vacancy H	a = 9.4537 c = 6.9916	4.92	+0.32	½ occupied 0.1	4.82
Vacancy O from OH	a = 9.4539 c = 7.0028	5.15	+0.55	Full occupied 0.1	5.05
Vacancy OH	a = 9.4883 c = 7.0018	5.49	+0.89	½ occupied band 3.11–3.82 with peaks 3.40 3.53 3.66	band 2.38–1.67 peaks 2.09 1.96 1.83
Interstitial H	a = 95013 c = 6.9842	5.12	+0.52	½ occupied peaks 1.20 1.45 1.75	peaks 3.92 3.67 3.37

As a result, photo-luminescence could be observed in this case, after preliminary excitation of electrons from the valence band to the conductive band (similar to experiments with the synchrotron technique [33, 34]). Moreover, as was established in reference [34], all HAP samples contain the same levels generated by OH vacancies, so as in paper [47], where OH vacancies arise due to the same preparation technology. However, using only PEE these

energy levels cannot be easily observed, due to their low intensity. With interstitial OH, the calculations show that for one unit cell model, the energy levels lie more closely (approximately twice as close) to the top of the valence band ($E_i \sim E_v$ + (1.48–2.07 eV), and also have an unoccupied energy level at ~ 2.4 eV. The energy gap, E_g, is more narrow in this case as well ($E_g \sim 4.24$ eV) by approximately –0.36 eV.

Another very interest and important result of these computational studies is that: it can be seen that H interstitials create three close, half-occupied energy levels with $E_i = E_v + 1.20$, 1.45 and 1.75 eV (Fig. 12,b, lower DOS image), and all with rather high intensity – approximately half of the D peak intensity. It means that existence of these energy levels due to H interstitials leads to the opportunity of the high concentration of electrons trapped on these levels. These levels can arise in HAP samples after hydrogenation procedures under high pressure or microwave irradiation, and can serve as traps for electrons as mentioned in [33, 34]. Therefore, these levels could serve for negative charges accumulation in the region of these inserted hydrogen atoms or protons.

2.4. Exploration of influences of various atoms substitutions in HAP structure and properties

Based on previous investigations of HAP structures the study of the influence on the HAP properties of the substitutions of various atoms in the HAP unit cell lattice structure were performed and described in details in papers [32–35]. Modeling and calculations were limited by the main peculiarity of the Mg, Sr or Si atoms as substituents in HAP structure is that they do not create any new electron energy levels inside the forbidden zone E_g of hexagonal HAP unit cell structure. They only result in a shift of E_g width value, and therefore a change in the electron work function ϕ. But, when Ca atoms were replaced by Mn and Se (which are often present in biological HAP) new energy levels, E_i, were observed to arise inside the forbidden zone E_g, in comparison with the initial pure HAP. In this case additional energy levels (E_i), occupied by electrons, arise inside the forbidden zone E_g, with very high intensities (I), which can serve as additional excitation centers during photoelectron emission experiments, making a contribution into the emitted electron flow. However, the most interesting results were obtained when considering atom substitutions in a HAP unit cell with an existing OH vacancy. In the latter case the data show that the E_g shift is larger for all atomic substitutions (Mg or Sr for Ca, and Si for P) when combined with OH vacancies, than that without OH vacancies. The data for atomic substitution of Ca by Mn or Se, with OH vacancies for complex substitutions in combination with OH vacancy, leads to arising of an additional half-occupied narrow energy band.

It means that in the model proposed, OH vacancies influence such substitutions which is in good agreement with experimental data presented in [35] for similar HAP samples. It is known, that in experimental HAP samples OH vacancies occur in high concentration [31, 60]. The data are similar for Mn and Se atoms. The E_g shift (in this case both without and with OH vacancy) leads to a change in the energy of electrons excited from occupied energy levels E_i, and thus to the experimentally observed shift of the electron work function, $\Delta\phi$, for these prepared HAP samples [35].

2.5. Oxygen vacancy in phosphate PO4 group of HAP

It is important to note here that recent studies and computational modeling using both approaches AIMPRO and VASP, have clearly shown that the oxygen vacancy in PO_4 group of HAP leads to strong additional occupied electron energy levels of ~ 3.45 eV inside forbidden band E_g [73, 74]. Therefore this oxygen defiance in the phosphate group creates a new optical absorption in ultraviolet spectral region, and leads to the photocatalytic activity observed in this material under UV light. This HAP has a sky blue color, attributed to oxygen vacancies, showing that it also absorbs slightly in the visible region. Moreover, modeling predicts that a

vacancy of OH group alone leads to a shift of the band gap into green and red region, with E_g in the range of 2.4–1.6 eV (521–743 nm). If this type of specific vacancy could be induced, it could lead to a novel visible-light photocatalyst or optical material.

All these studies are devoted to modeling of several imperfections in the initially perfect bulk HAP. But for investigation of the HAP interactions with living cells, etc., it is necessary to study the models of surfaces of initially perfect HAP crystals. And further, on the next stage, to investigate various models of defects, which can arise on the HAP surfaces.

3. FIRST PRINCIPLE STUDIES HAP NANOSTRUCTURED SURFACE PROPERTIES

3.1. Main principles and features of HAP surfaces, charges and electric potential images

Using the data obtained for optimized HAP unit cell lattice atomic positions in first principle AIMPRO calculations we can construct HAP crystal structures consisting from several unit cells and cluster models of various sizes for hexagonal and monoclinic phase.

The initial lattice unit cell for hexagonal HAP structure consists from 44 atoms (Fig. 1), while for monoclinic HAP nanostructures it consists from 88 atoms (Fig. 3), because the lattice unit cell is doubled in this last monoclinic case along *b* axis [9, 11, 32, 113]. One of the main features, which we must remember is that in the repeated unit cell for construction of such periodically repeated crystal structure in each unit cell, only one OH-channel consisting from 2 OH molecular groups must be present (Fig. 1, Fig. 2).

In works [30−35] for creation and reconstruction of every biggest crystal cluster consisting from several unit cells the HyperChem workspace [55] was used. The unit cell structure with 44 atomic positions was transferred from AIMPRO [52] into HyperChem format. This allowed us to obtain several various crystal structure models of HAP crystal with different sizes in various directions (Fig. 13,a and Fig. 14), which reveal different open surfaces.

For comparison of all models with basic theory [32–34, 57]. Fig. 13,b shows several axes and planes for HAP structures: Projection in [001] direction showing the two $(10\bar{1}0)$ surfaces (planes) relative to the position of the two fold screw axes and centers of symmetry. Of the six fold screw axis (6_3) only the sub-group 2_1 is relevant.

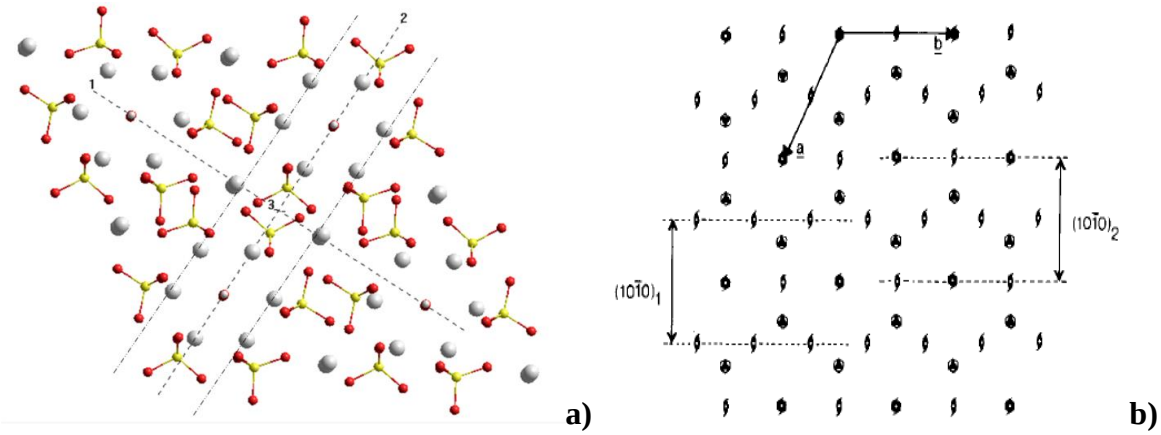

Fig. 13. Different planes and axes for two type positions of Ca atoms with various distances between Ca atoms: a) from our HyperChem modeling; b) an example from [57].

Computational modeling using HyperChem tool allows us to study in greater detail both structural peculiarities of HAP, and their surface charges as well as electrostatic potential distributions [32]. Some of the studied HAP structures are presented in Fig. 14.

It was clearly shown that Ca atoms exist here in two main different positions (Ca1 and Ca2), with different distances between them in several directions. This positioning of Ca atoms determines the specific charges and electrostatic potential distributions on the corresponding and different HAP surface.

Such variation of HAP surfaces with different Ca atoms positions could be revealed in the interactions with outer space and with any charged species presented in surrounded media, such as citrates. It should be pointed out that for various open surfaces with different concentrations of positive Ca atoms and negative O atoms, different surface charges and electric field distribution could exist (Fig. 15).

As is seen from Fig. 15 the main HAP surface covered with Ca atoms creates the positive surface charges and positive electrostatic field counter, while, if oxygen O atoms or the OH group molecules occur on the HAP surface, the negative surface charges prevail here and negative electrostatic field counter line exists around this surface.

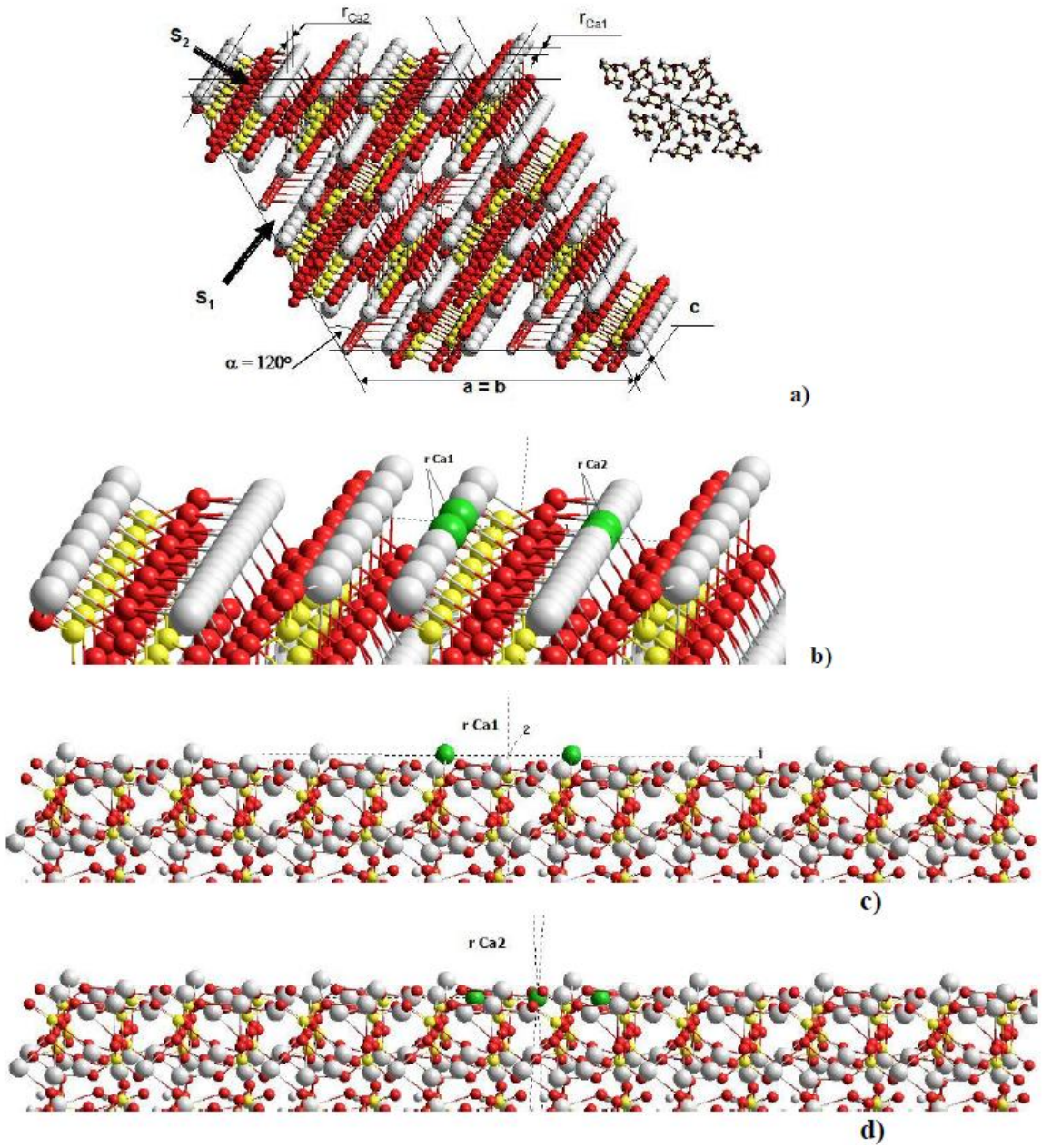

Fig. 14. Molecular model of HAP cluster constructed in HyperChem workspace on the basis of preliminarily optimized crystal structure and all atomic positions: a) iso-projection image; b) main Ca positions on HAP surface; c) and d) positions of main Ca1 and Ca2 atoms on HAP surface.

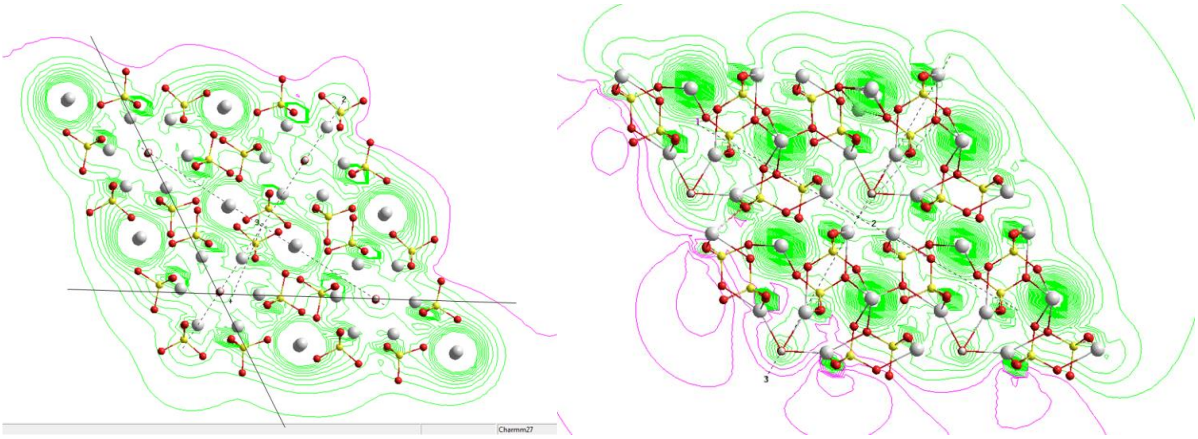

Fig. 15. Electrostatic field distribution at the HAP crystal surface structures with different outer open planes and consequent various charges on open surface. Green color – positive electric field, red – negative.

Therefore, any negative charge, such as frequently used citric acids or citrates molecules, could be easy attached directly on these sites on the HAP surface where the positive Ca atoms are positioned [31, 32]. As is known, citrate molecule has a negative total charge $q_C = -3$. In works [31, 32] several models for adhesion of citrates on various HAP surfaces were constructed and studied. After optimization by PM3 it has a different distribution of effective atomic charges, with the main part of negative charges being concentrated on the oxygen atoms. After further optimization of citrate molecule position on HAP surface, the average distance of citrate molecule from HAP surface is ~ 3–4 Å [30–32].

From experimental studies of the influence of citrates on the HAP nano-crystals formation it is known now, that for different contents of citrate molecules in the initial starting solution for precipitation of HAP, in the course of growth the HAP structure acquires different sizes, lattice's parameters and shapes [30, 45]. The data obtained show clearly the positioning of interacting sites on the HAP surface and allow us to propose a mechanism for the formation of various HAP nanostructure shapes under the influence of negatively charged citrate quantities. It is similar to HAP NPs size and shape variations [30] in the course of their interactions with hydrogen atoms (protons), but having positive charges.

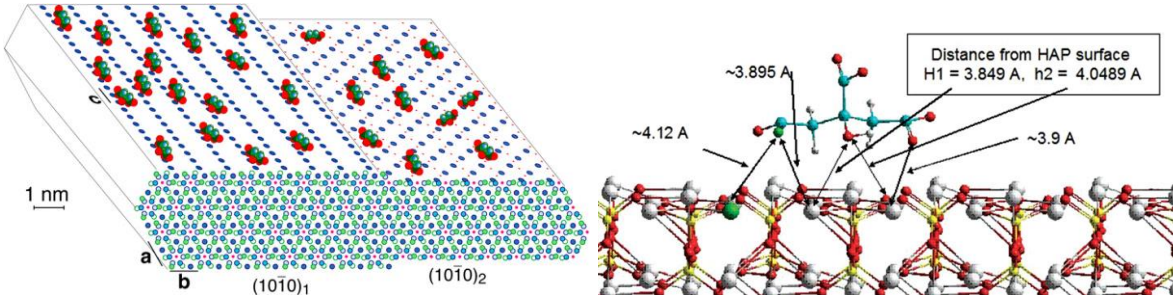

a) **b)**

Fig. 16. Scheme of apatite-bound citrate (with oxygen of the carboxylates in red) interacting with Ca^{2+}: a) view on two surfaces of high morphological importance of a bone HAP nanocrystal, where multinuclear magnetic resonance (NMR) analysis reveals that bound citrate accounts at a realistic citrate surface density of 1 molecule per $(2\ nm)^2$, with its three carboxylate groups at distances of 0.3 to 0.45 nm from HAP surface [59] (calcium ions are blue filled circles on the top and front surfaces, P is green (omitted on the top surfaces), OH^- ions are pink dots, while phosphate oxygen is omitted for clarity); b) optimized molecular model for positions of citrate molecule in relation to HAP Ca-surface on the distance 3.9–4.2 Å [31, 32] (printed with permission from IEEE and Copyright Clearance Center [32]).

Citrates have the same influence on the shapes of HAP, which can bound and stabilize the HAP structures by various adhesion features on different surfaces, as it was shown by AFM technique (Fig. 16,a) [58, 59]. It was confirmed by molecular modeling [31, 32], where interactions of citrate molecules with HAP surface was studied (see Fig. 16,b).

Depending on the initial ratio [cit:Ca] from = 3:1 up to = 7:1, the final citrate surface density was in the range from ~ 0.76 ions/nm^2 up to ~ 1.05 ions/nm^2. As it was shown in [31, 32, 45], in the former case after synthesis and growth of HAP in the presence of citrates the HAP nanorods were short of the length of ~ 100 nm, while in the latter case the nanorods were longer of length up to ~ 1000 nm. Therefore, it was shown that citrates stabilize the HAP surfaces and shapes (due to their charges, just as hydrogen charges or protons influenced HAP NPs shape [31, 32]).

The data on HAP interactions with citrates show the positioning of interacting sites on the HAP surface, and allow us to propose a mechanism for the formation of various HAP nanostructure shapes under the influence of varying citrate quantities. Modeling, performed in [31, 32], shows that H-bonded citrate pairs cover and stabilize the HAP nanostructures.

In recent experiments by atomic force microscopy (AFM) using functionalized tips, it has been found that pure HAP mineral surfaces are close to isoelectric at pH = 6 with negative surface charge average of −0.02 C/m^2 and varying between −0.0037 and −0.072 C/m^2 [60], Fig. 17. This result is correlated with that considered for monoclinic ordered HAP [43], where the polarization values of the same order 0.0038 C/m^2 were obtained. Note, that similar polarization (in absolute values) was estimated on the order of ~ 0.005 C/m^2 for various type of HAP NPs [30] (see Table 3), the other measured data 0.072 C/m^2 is close to the value for HAP crystal structure ~ 0.1 C/m^2 estimated in works [13–15, 28, 29], and computed for minimal sized HAP cluster (see Table 4) [30]. These data are comparable with the biggest known measured value 0.149 C/m^2 by Nakamura [12], and it is only twice lower in average.

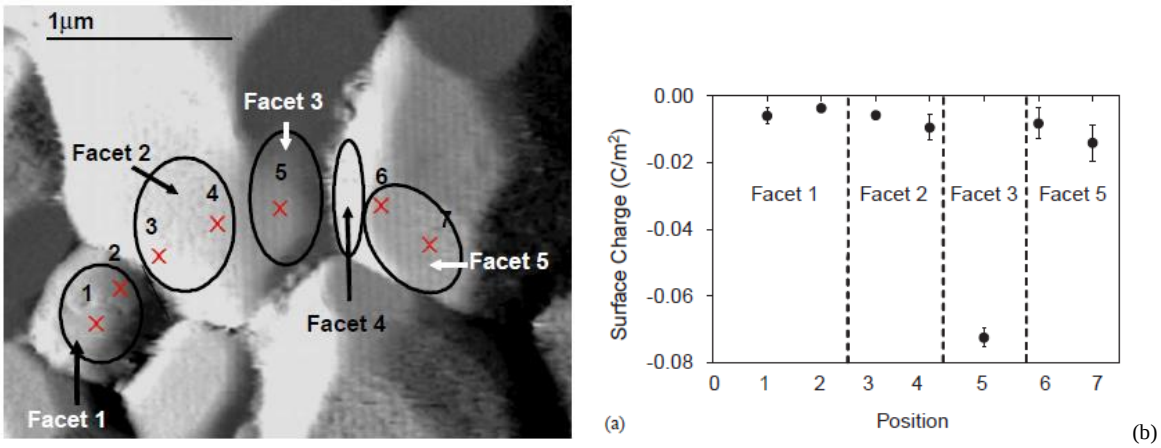

Fig. 17. Different facets among the grains: a) imaged in Scan by AFM; b) approximation of surface charge per unit area [60] (reprinted with permission from [60], Elsevier Ltd and Copyright Clearance Center).

Here we should make some remarks on the results, which were obtained in work [61]. There a very small surface charge (0.000033 C/m^2) was registered under the following poling conditions: E_p = 400 V/mm ~ 400 kV/m, T_p = 350 C, and t_p = 60 min, which is two orders lower than the above values [30, 43, 60] and almost four orders of magnitude smaller than the values of 0.1–0.149 C/m^2, (under similar poling condition E_p = 100 kV/m, T_p = 400 °C, t_p ~ 1 hour) [12]. The latter result was obtained by thermally stimulated depolarization current (TSDC) measurements, and is comparable with other above estimations [13–15, 28–30]. The result obtained in [61] is very strange, but the authors argued that a possible reason for this great discrepancy could be, the overestimated dipole polarization determined from TSDC

measurements. But the latter measurements account for some types of volume polarization effects, polarization arising from trapped charges at grain boundaries. The other possible reason is that the observed surface charge is the alignment of OH-ions which cannot be directly observed. A similar discrepancy (a considerable difference between the surface charge and polarization effects) was reported by Johann and Soergel in a ferroelectric material [61, 62]. They proposed that some charges from the surroundings adsorbed on the surface, thereby subsequently masking the effective surface charge. Such masking effects may be responsible for the difference between surface charge and polarization. All these questions need further investigations and detailed clarifying insight.

Finally, it is also worth noting, that the value of the polarization and the surface charge density (P ~ 0.0038 C/m^2) obtained in view of the general law of the electromechanical coupling (that is the connection between polarization and piezoelectric coefficients, inherent of all ferroelectrics) [63, 64] leads to the value of the piezoelectric coefficient of the order of d ~ 15.7 pm/V, which only twice larger than values ~ 7.62–8.48 pC/N (or pm/V) measured by Halperin et al. on tibia bone samples by piezoresponse force miscroscopy [64, 65]. As we discussed above (section 2.2) such deviation could occur by averaging the registered piezoelectric signal from different grains with various local polar states, fluctuated in cross-section of the native tibia bones samples. But the most important conclusion is that the distribution of negative surface charges with average value at the level of –(0.1–0.0038) C/m^2 is just responsible for these effects.

Therefore, we must emphasize here, that on different open HAP surfaces various breaking and dangling chemical bonds (from OH, PO4, Ca atomic groups) arise, which have different charged states and signs. Such situation occurs for an ideal perfect HAP structure, but it leads to many new surface defects too, including possible adhesion of some atoms from surrounding medium, water molecules, etc. So, it is necessary to consider in greater detail just the perfect HAP surface features, which are most important for creation of surface electrical charges and potential with corresponding sign. Further we consider here contemporary existing models and computational procedures allowing us to estimate quantitatively these HAP surface electrical properties.

3.2. Super-cell and slab approaches for HAP surface-vacuum nanostructure modelling

To study more detailed HAP surface properties it is necessary to be aware of which of the actual surfaces of HAP structure we want to investigate. As we have seen above from modeling of various sizes and shapes of HAP clusters, several different surfaces could represent the HAP sample at the interface with the surrounding open space (or vacuum). Each of these surfaces has other electrical properties, charges and fields, and as result – different electron work functions.

First, for correct modeling consideration is usually given to several most commonly used HAP surfaces. Various authors use different approaches, but mainly surfaces with Miller indexes (001), (101) and (010) were studied, which represent the plane perpendicular to the corresponding direction [001], [101] or [010] (Fig. 18) [66].

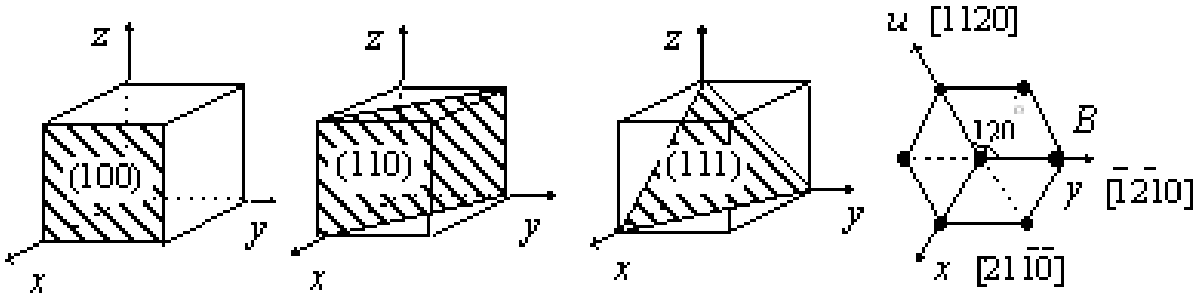

Fig. 18. Scheme of Miller's indexes for crystal surfaces.

For hexagonal structures the use is often made of indexes, including 3 coordinate axes [*uxy*] in the plane (0001) perpendicular to the *OZ* axis (Fig. 18, last image), the (1010) and (1000) eventually used for hexagonal structures.

For example Figures 19–22 show HAP structures with such direction and planes from Astala & Statt paper [24], Rulis et al [26] and Slepko & Demkov [23].

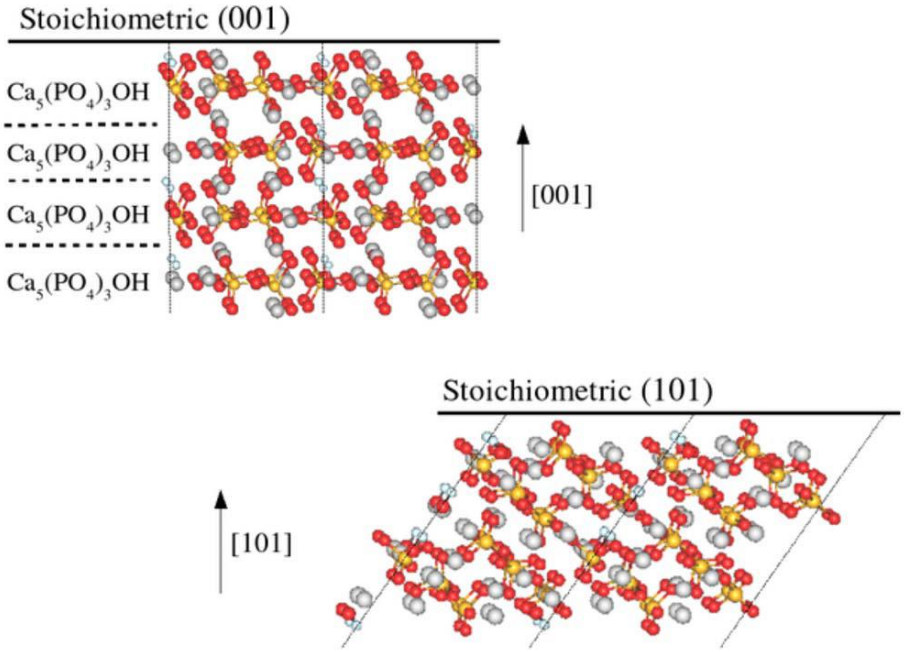

Fig. 19. A side view of the stoichiometric (001) and (101) slabs. Multiple unit cells of the periodic structure are shown. Tetrahedral groups are PO_4 ions, large spheres are Ca atoms, and small spheres are H atoms. For the (001) surface, the $Ca_5(PO_4)_3OH$ layers have been highlighted. Orientation of OH ions in the channel, which breaks the symmetries between the tops and the bottoms of the slabs (printed with permission from APS and Copyright Clearance Center [24]).

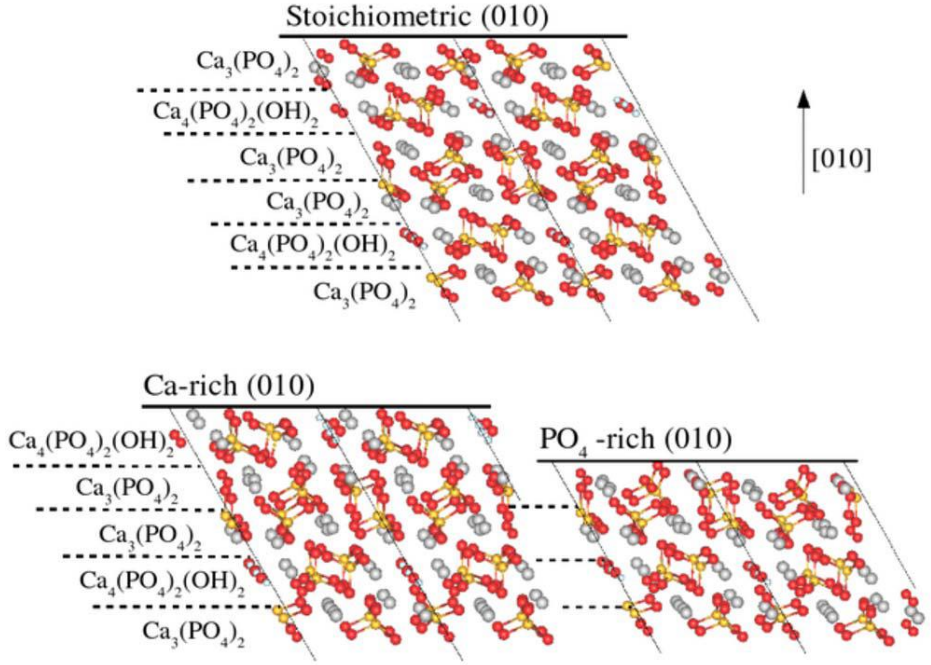

Fig. 20. A side view of the (010) surface slabs. Multiple unit cells of the periodic structure are shown. The layered structure is highlighted (Printed with permission from APS and Copyright Clearance Center [24]).

The second important remark is that various surfaces, corresponding to some layers in HAP structure, can have various stoichiometric contents and the value of ratio of Ca/P can differ from value = 1.67. For example, such situation is shown in Fig. 19, 20 from Astala paper [24]. As is seen, such structure is very similar and comparative with formation of HAP cluster in Onuma paper [41] (see Fig. 3,a) and close to the growth of the minimal cluster from Bystrov paper [30] in *OZ* axis direction along OH-channel (Fig. 2).

Third, an important feature of surface properties modeling and calculations of their electrical field and charges properties by using various contemporary first principle and DFT methods, and corresponding software, is that the HAP structure is presented as a layered slab supercells unit, with includes vacuum spaces between the layered slabs.

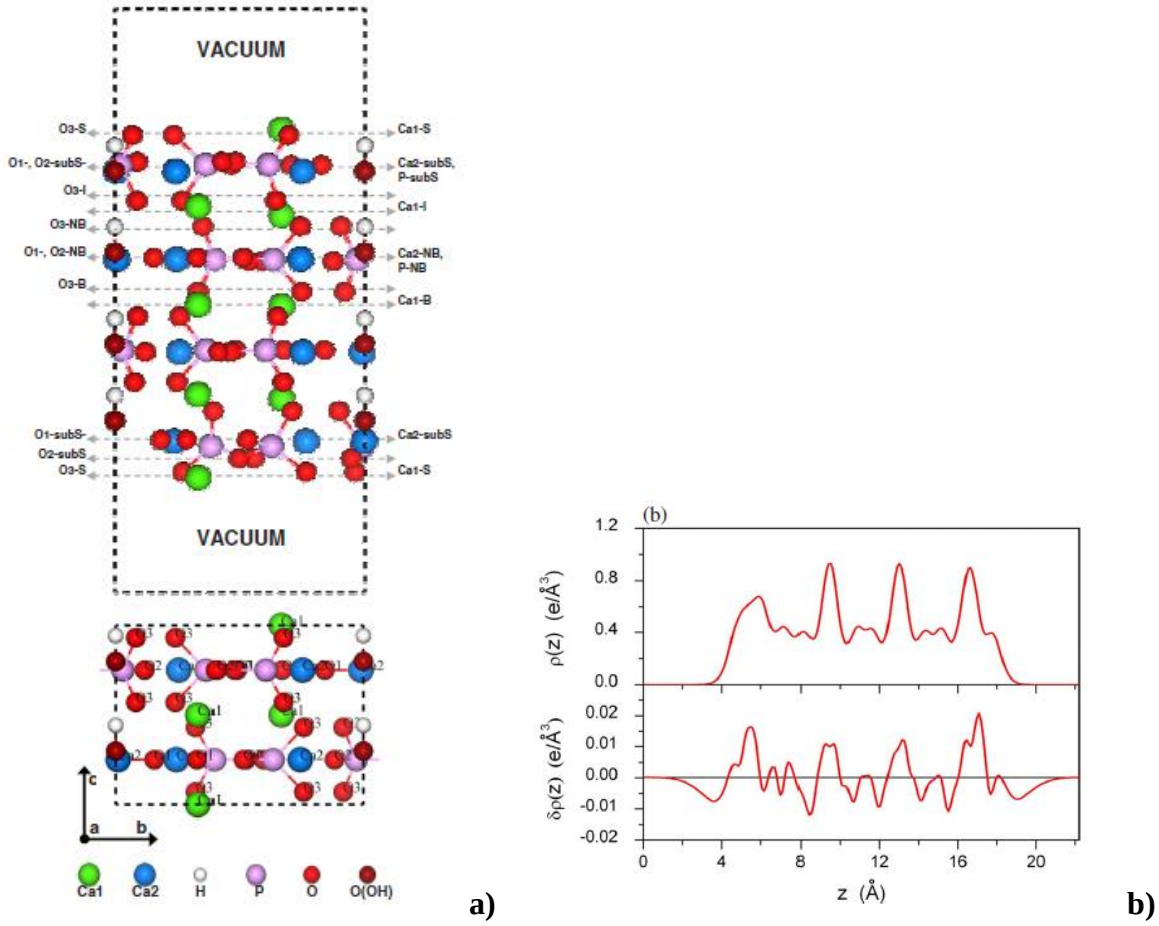

Fig. 21. Relaxed surface model of HAP (001): a) layers of atoms are labeled as explained in the text (the lower part shows the corresponding crystalline layers); b) electron charge density ρ(r) and δρ (r) across the bulk and surface in HAP (001) (Printed with permission from APS and Copyright Clearance Center [26]).

One example of such approach is shown in Fig. 21 from Rulis paper [26]. A similar super-cell construction is used as an initial model for various authors, and then performed for structural optimization using different DFT methods such as local basis (LDA) [35, 52–54] and plane-wave (general gradient approximation: GGA) [22, 23, 67, 68] (or VASP) codes. Of course, in any case for the initial perfect and pure stoichiometric unit cell of hexagonal bulk HAP, the model [35] shown in Fig. 1 is used. Note that since hexagonal and monoclinic phases are energetically close (as was pointed out in several works [22, 24, 32, 34, 35, 43, 67]), in all such cases of surface property studyes many authors use only the simplest case of hexagonal phase.

A similar presentation of modeled HAP slab structures with the vacuum spaces on surface plane was used in Sleko & Demkov works (Fig. 22) [22, 23, 67]. (Note, that they used four indexes to mark HAP hexagonal plane surfaces in their work [23]).

Let us consider firstly the paper of Astala & Statt [24]. The bulk HAP used has a hexagonal structure consisting of layers of PO_4 groups and Ca ions and of OH ions that occupy channels running along the *c* direction (see Fig. 19, Fig. 20). The lattice parameters observed and used here are a = 9.42 Å and c = 6.89 Å. [24]. These data are close to the data of other authors (Table 1, Table 5) [4, 10, 21, 26, 35].

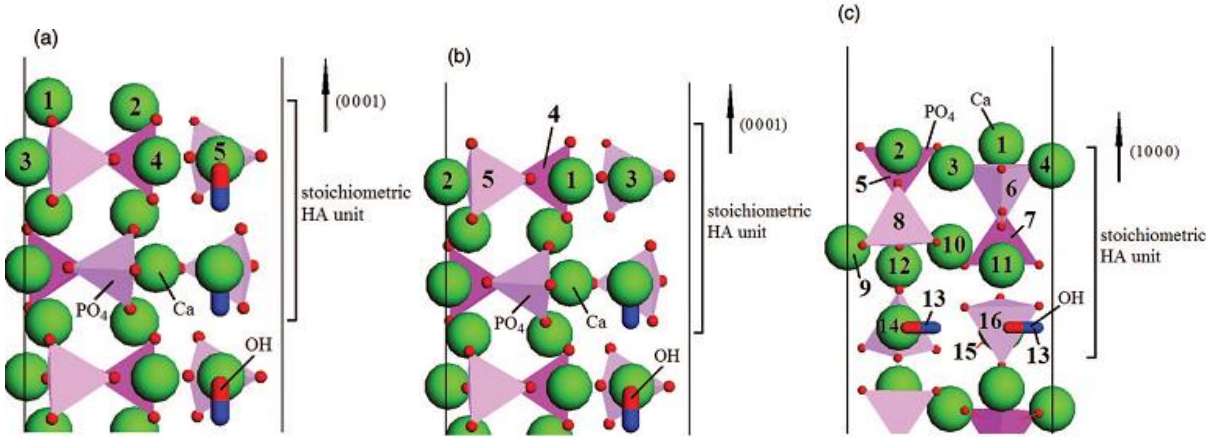

Fig. 22. Three prototypes of HA surface structures. From these three models they derive all other model surfaces by continuously removing the numbered particles. In total, they construct 29 surface models from the ones depicted. The classifications of the surface models are listed in Table 1 (Printed with permission from AIP Publishing LLC and Copyright Clearance Center [23]).

Supercells, which are periodic in three dimensions, were used in these calculations. Three different surface facets were considered: (010), (001), and (101). The surfaces were modeled using slabs cut from bulk HAP so that the crystalline periodicity in the in-plane directions was retained. In the normal direction, the slabs were separated from their periodic images by vacuum layers of 17 Å thick or more, which is enough to make the interaction between the slabs negligible. The model surfaces were constructed so that the slabs were charge neutral.

Since the breaking of P-O or O-H bonds is likely to be energetically costly, the surface cuts were chosen so that PO_4 and OH ions were left intact. In the (001) and (010) directions, the structure consists of layers providing natural cuts that maintain charge neutrality (Fig. 19 and 20).

In the (001) direction, all these layers have the same stoichiometric composition of $Ca_5(PO_4)_3OH$. Note that because the OH ions are aligned in the (001) direction, there are two slightly different (001) surfaces, depending on the OH orientation. In the considered slab model, the top and the bottom of the slab have different OH orientations.

Here we must emphasize that quite similar situation is considered in Rulis et al. paper [26], where the finally optimized super-cell slabs structure is shown in Fig. 21,a: it is the principal peculiarity of the HAP- and OH-groups formed OH-channels structure, but each OH dipole orientation has an important role, and on the different sides of slabs OH have different direction.

Below this point will be considered in greater detail. But here we shortly comment for comparison the data obtained from Rulis et al. [26].

The atomic displacements of all atoms from the original initial crystalline positions after optimization are obtained and analyzed [26]. In particular, different displacements between the upper and lower surfaces of the HAP model indicate a strong influence of the OH position in HAP (001). The Ca1 ions on the surfaces move outward-toward the vacuum in HAP (001) model. In HAP, the outward displacement is larger at the upper surface than at the lower surface. There are considerable lateral movements of the Ca ions in the subsurface and

intermediate regions. The displacements become much smaller in the layers near the bulk region and become negligible for the bulk atoms.

It should also be noted, that for all the models used one important limitation of the periodic supercell approach is that the surfaces must remain charge neutral to avoid diverging electrostatic energy. If the HAP is immersed in a fluid, the surface charge will depend on the pH of the fluid, and therefore, the charge neutrality constraint implies, in particular, a fixed pH. However, we repeat and emphasize that, in recent experiments by atomic force microscopy using functionalized tips, it has been found that pure HAP mineral surfaces are close to isoelectric at pH = 6 with negative surface charge average of -0.02 C/m^2 [60]. At most, this implies one unit of negative elementary charge per two or more surface cells. This being so, the charge neutrality constraint represents reasonable physical conditions.

Let us consider more carefully Astala & Statt models. For the (010) direction, there are two different types of layers. First, there are A-type layers composed of $Ca_3(PO_4)_2$ that have a Ca/P ratio of 1.5 and are therefore PO_4 rich compared to stoichiometric hydroxyapatite with a Ca/P ratio of 1.67. Second, there are B-type layers of $Ca_4(PO_4)_2(OH)_2$ that have a Ca/P ratio of 1.75 and are therefore Ca rich. This approach forms the AABAAB stacked structure so that cutting between the layers yields three chemically distinct terminations (Fig. 20). The ABA termination is stoichiometric one. Removing the outmost A-type layer gives BAA termination, which leaves the slab Ca rich because the PO_4-rich layer has been removed. Finally, removing the Ca-rich B-type layer gives AAB termination and a PO_4-rich slab. Such way leads to three different (010) surface facets that are denoted respectively stoichiometric, Ca-rich, and PO_4-rich. These are important features of HAP slabs layered structures revealing various surfaces. These peculiarities were used by other authors too.

Note, that in Astala & Statt paper [24] the construction of surface slabs began by taking single unit cells of HAP that had both the lattice parameter and atomic coordinates relaxed and then stacking these cells in the surface normal direction. The stoichiometric slabs had two HAP unit cells stacked in the surface normal direction. The nonstoichiometric (010) surfaces were constructed by starting from the stoichiometric two-cell slab and cleaving off layers from the top of the slab. It is noteworthy that the thicknesses of slabs (10–16 Å) are close to that of natural bone platelets (15–40 Å). On the Ca-rich (010) surface, the topmost Ca atoms can have two different positions; both cases were investigated.

The (101) surface was constructed in the same way as the other surfaces by cutting a stack of HAP unit cells. Only one surface cut was found that yielded a stoichiometric charge neutral slab without broken P-O or O-H bonds. With (101), there are again two slightly different surfaces due to two possible OH orientations.

Noteworthy is that in all the model cases the authors used the first-principles and DFT techniques for the total energies and forces calculation. For the optimized surface studies, all the authors used various Geometry optimization methods, where the positions of all atoms in the slabs were relaxed using a conjugate gradients algorithm or similar (see details in [22, 24, 26, 35]). The lattice parameters in the surface plane were held fixed at the calculated bulk values (for example: $a = 9.36$ Å and $c = 6.99$ Å). But in some cases the lattice was optimized too [35]. The super cell dimensions in the directions normal to the surfaces were held fixed at large values, as described above. No symmetry constraints were imposed at any stage.

Note also that a similar constructions and destinations between slabs in super-cell models are widely used. For example, in Rulis paper [26] fully relaxed (001) surface models for HAP are shown in the upper portions of Fig. 21,a. After relaxation, the cell dimensions for HAP (001) are $a = b = 9.4320$ Å and $c = 22.1992$ Å. For the HAP (001) model, the symmetry of the two surfaces (upper and lower) is broken due to the orientation of the OH group on the c axis. As a result, the upper and the lower surfaces in HAP (001) are slightly different.

In Rulis model [26] (Fig. 21): the Ca, P, and O ions in the HAP (001) model are labeled in this case; there are several types of labels because of the difference in the upper and lower surfaces. Accordingly, the Ca ions are labeled as Ca1-S-upper, Ca1-S-lower, Ca2-subS-upper,

Ca2-subS-lower, Ca1-I, Ca2-NB, and Ca1-B. The O ions are labeled as O3-S-upper, O3-S-lower, O2-subS-upper, O2-subS-lower, O1-subS-upper, O1-subS-lower, O3-I, O3-NB, (O1+O2)-NB, and O3-B. Here notations S, subS, I, NB, and B stand respectively for surface, subsurface, intermediate, near bulk, and bulk, and first numeral denotes the species origin from the crystalline system. The P ions are divided into P-subS and P-NB. The OH groups differ slightly between the four (OH) ions in the (001) surface.

The displacements of all atoms from the original crystalline positions after relaxation are important for analysis. Upon analysis, these data show large differences in the atomic relaxations between HAP surface models. In particular, different displacements between the upper and lower surfaces of the HAP model indicate a strong influence of the OH position in HAP (001). The Ca1 ions on the surfaces move outward-toward the vacuum in HAP (001) models. In HAP, the outward displacement is larger at the upper surface than at the lower surface. There are considerable lateral movements of the Ca ions in the subsurface and intermediate regions. The displacements become much smaller in the layers near the bulk region and become eligible for the bulk atoms. Many shifts and rotations of all atomic positions after relaxation were analyzed by the authors.

But, the key features of the relaxed structure of HAP (001) are due to the effects of the different c-axis ions in a system. Further, the differences between the upper and lower surfaces in HAP (001) are related to the fact that the OH group is a polar bond and thus has a distinct orientation.

Finally, Rulis [26] obtained the surface charges distribution (see Fig. 21,b). It is interesting, that from first principles viewpoint, HAP surface could have various charges, because HAP surface has both positive and negative charges due to the charged Ca^{+} ions and PO_4^{3-} groups. But, on the other hand, it is very important, as was revealed via charge density calculations, that HAP crystals are mostly positively charged, because of the Ca^{+} ion presence over the surface. Therefore, the water and other organic molecules are involved in the absorption which is perfectly seen on charges profiles calculated [26]. So, it was [26] directly shown that the HAP surface must be most positively charged in the region of Ca ions close to the surface. Note here that above we discussed this situation for Ca ions on HAP surface. But, on the other hand, a possible surface charges distribution depends also on which crystallographic surface a real HAP surface occurs, which may be arranged with negative oxygen ions too. And moreover, we must take into account that in a real situation we have not a crystallographic homogeneous sample, but ceramics consisting from many small micro-crystals with stochastically different orientations located in close proximity. And this leads to irregularities on the common HAP samples surface.

And opposite sides of the model HAP slab have differences in charges due to difference of the orientation of the OH groups with corresponding dipole orientation along axis of the OH-channel.

A similar to Rulis [26], but more detailed analysis was made in Astala [24] and Slepko [22, 23]. But there are some differences between them. Let us consider now some more details from Slepko & Demkov [22, 23, 67]. They made a similar simulation cells of the size 10 Å × 10 Å × 40 Å. These models consist of 15–20 Å thick slabs separated by a 20 Å thick vacuum region in the *c*-direction to suppress interactions between neighboring cells when applying periodic boundary conditions.

The surface models are built in a quasi-symmetric fashion to prevent the macroscopic electric fields across the slab. By quasi-symmetric we mean that the atomic compositions of the top and bottom surfaces are the same. However, as a consequence of the low crystal symmetry, the PO_4 molecules and Ca atoms on the surface planes may be rotated and translated with respect to each other. Only in the (0001) models, a deviation from this rule was observed as there the OH groups have hydrogen pointing towards the bottom surface and oxygen pointing towards the top surface (Fig. 22,a). In these models the top and the bottom

surface of each model differ in the orientation of OH groups. Further the authors of [23] studied the surfaces with (0001) and (1000) (or with (001) and (100)) crystallographic orientations, allowing for both stoichiometric and non-stoichiometric models. By stoichiometric model here it mean that the model slab contains an integer number of HA formula units. The considered surface terminations must keep the OH and PO_4 groups intact. In total, they constructed twenty nine distinct atomic level surface models. Three of them are depicted in Fig. 22.

Table 7. Chemical composition, ionic charge, the surface energy averaged over the entire chemical range and work function of models [23, 67]. The sub-indices indicate the stoichiometry of the models. Ionic charge: Negative stoichiometry indicates P-rich conditions, while positive stoichiometry indicates Ca-rich models. The extra molecules indicate the deviation from HAP bulk stoichiometry measured in numbers of OH, PO_4 or Ca. The net ionic charge is simply the sum of the extra elements multiplied by $-3e$, $-1e$ and $+2e$ for PO_4, OH and Ca, respectively. In the case that several terminations exist with the same stoichiometry, upper indexes are used to differentiate the models (Modified and printed with permission from AIP Publishing LLC and Copyright Clearance Center [23])

Model number	Model type	extra OH	extra Ca	extra PO_4	ionic charge [e]	av. σ^a [eV/Å^2]	ϕ^b [eV]
1	$(0001)_{+4}$	0	2	0	4	0.09	3.1
2	$(0001)_{0}$	0	0	0	0	0.06	5.5
3	$(0001)_{-4}$	1	3	3	–4	0.10	7.5
4	$(0001)^{1}_{-8}$	1	1	3	–8	0.20	9.0
5	$(0001)_{-12}$	2	4	6	–12	0.28	8.6
6	$(0001)_{-16}$	2	2	6	–16	0.38	9.1
7	$(0001)^{1}_{-2}$	0	8	6	–2	–0.09	7.3
8	$(0001)_{-6}$	0	6	6	–6	–0.02	7.8
9	$(0001)_{-10}$	0	4	6	–10	0.06	8.5
10	$(0001)_{-14}$	0	2	6	–14	0.14	9.1
11	$(0001)^{2}_{-8}$	0	2	4	–8	0.31	8.0
12	$(0001)^{2}_{-2}$	0	2	2	–2	0.03	7.2
13	$(1000)^{1}_{+4}$	0	8	4	4	–0.05	3.0
14	$(1000)^{1}_{0}$	0	6	4	0	–0.09	5.7
15	$(1000)^{1}_{-4}$	0	4	4	–4	0.00	7.2
16	$(1000)^{1}_{-8}$	0	2	4	–8	0.09	7.7
17	$(1000)_{-12}$	0	0	4	–12	0.18	8.6
18	$(1000)_{-6}$	0	0	2	–6	0.13	8.8
19	$(1000)^{2}_{0}$	0	0	0	0	0.08	7.1
20	$(1000)_{+6}$	1	5	1	6	0.23	4.4
21	$(1000)_{+12}$	2	10	2	12	0.37	3.3
22	$(1000)_{+8}$	2	8	2	8	0.31	3.1
23	$(1000)^{2}_{+4}$	2	6	2	4	0.25	3.3
24	$(1000)^{3}_{0}$	2	4	2	0	0.20	5.1
25	$(1000)^{2}_{-4}$	2	2	2	–4	0.62	9.7
26	$(1000)^{4}_{0}$	0	12	8	0	–0.23	6.7
27	$(1000)^{3}_{-4}$	0	10	8	–4	–0.14	7.6
28	$(1000)^{2}_{-8}$	0	8	8	–8	–0.05	8.8
29	$(1000)_{-2}$	0	8	6	–2	–0.12	7.6

[a]av. σ is the average value of surface energy obtained for each cases,
[b]ϕ is the electron work function

Three prototypes are shown in Fig. 22. The numbers in Fig. 22 indicate how they cleaved these models. For example, removing particle 1 in Fig. 22,a yields a new model, removing particles 1 and 2 yields another one, and so on. From the model depicted in Fig. 22,a the authors deduced a total of six atomistic surface models (1–6 in Table 7), from Fig. 22,b a total of six surface cleavages (7–12 in Table 7), and from Fig. 22,c they deduced a total of 17 models (13–29 in Table 7). The deviation in stoichiometry from HAP bulk is denoted in Table 7 by a sub-index, where the positive sub-index denotes Ca-rich model, and the negative sub-index denotes P-rich model – as in Astala work [24]. To indicate by how many OH, Ca and PO_4 formula units used models deviate from the HA bulk stoichiometry and the bulk ionic charge per cell for each model [67] see in Table 7. The bulk ionic charge is calculated by assigning formal charges $-3e$, $-1e$ and $+2e$ to the PO_4, OH and Ca chemical units, respectively. Overall, the models are charge neutral. To differentiate between models with same stoichiometry here authors used an upper index. The authors considered a wide range of Ca-rich and Ca-poor models to account for the large Ca/P range of 1.3–1.9 found in natural bone [69].

The authors of [23, 67] obtained two stoichiometric models, one with the (0001) and one with (1000) orientation, and three more surfaces with zero bulk ionic charge.

In addition, they obtained models with a wide range of ionic charge between $-16e$ and $+12e$. As a consequence of such cleaving procedure, they only considered one surface with the positive ionic charge with the (0001) orientation. For example, in Fig. 24,b three top Ca atoms were successively removed before removing the phosphates to obtain the next surface model. This way the surface becomes increasingly negatively charged due to the $-3e$ charge of PO_4 groups. Experimentally, surfaces with net ionic charges are found to drive the HAP platelets growth kinetics [70] but are typically neglected in surface studies of HAP. Then the authors applied periodic boundary conditions and fully relaxed atomic positions. Finally all the models consist of 15–20 Å thick slabs separated by a 20 Å thick vacuum region in the c-direction to suppress interactions between neighboring cells.

Due to quasi-symmetry it means that on average, the atomic compositions of the top and bottom surfaces are the same. The PO_4 groups and Ca atoms of the two surfaces can be rotated and translated in the surface planes with respect to each other as a consequence of crystal symmetry. In the (0001) models, the OH groups were deviated from this rule and have hydrogen pointing towards the bottom surface and oxygen pointing towards the top surface (Fig. 22,a). In these models the top and the bottom surface of each model differ in the orientation of OH groups.

3.3. Surface charges and energy for various HAP surfaces with different stoichiometry

For calculation of the surface energy various the authors used some different approaches. In work [24] the authors start with a most simple equation. The surface energy E_{surf} for a slab of stoichiometric composition can be defined as the energy difference between the slab E_S and the equivalent number of bulk formula units E_B, divided by the surface area A,

$$E_{surf} = (E_S - E_B) / A \tag{2.1}$$

For the (001) and (101) surfaces, which have two different OH orientations, this formula yields an average. In order to define the surface energy in non-stoichiometric cases, here the authors of [24] assumed equilibrium conditions so that the chemical potential of each species of ion be equal to its value in some external reservoir. Thus, the energy to create a surface is the energy difference between the surface slab and the bulk, plus the energy to add or remove ions to reach the correct chemical composition. This chemical potential dependent surface energy can be similarly written as

$$E_{surf}(\mu[X_1],...,\mu[X_n]) = \left(E_S - \sum_{i=1}^{n} \mu[X_i] \right) / A, \tag{2.2}$$

where $\mu[X_i]$ is the chemical potential of ion species X_i, which can be estimated by using chemical potentials of appropriate bulk phases as references. Using bulk HAP one yields

$$\mu[\mathrm{HAP}] = 10\mu(\mathrm{Ca}) + 6\mu(\mathrm{PO_4}) + 2\mu(\mathrm{OH}). \quad (2.3)$$

At $T = 0$ K and $p = 0$ Pa, the $\mu[\mathrm{HAP}]$ equals $E_{HAP} = E_B$ the energy of a bulk HAP unit cell.

The authors considered here several different cases and denoted the surface energies of stoichiometric, Ca-rich, and PO_4-rich (010) surfaces as $E^{S}_{surf\,(010)}$, $E^{Ca}_{surf\,(010)}$ and $E^{P}_{surf\,(010)}$ respectively. After analysis of each surface using E_q (2.2), they concluded that it is possible to write the surface energies as a function of a single chemical potential variable

$$3\mu[\mathrm{Ca}] - 2\mu[\mathrm{PO_4}] = \mu[\mathrm{Ca_3(PO_4)_2}]$$

for an external reservoir that is in equilibrium with the surface.

Because the prefactors of $\mu[\mathrm{Ca_3(PO_4)_2}]$ differ (−1 for Ca-rich (010), +1 for PO_4-rich (010), and 0 for stoichiometric surfaces) the relative values of surface energies will depend on this variable. By producing a plot of the surface energies and tracing the lowest-energy envelope, the most stable surfaces can be found. Alternatively, the surface energies can be expressed in terms of a more familiar variable $\mu[\mathrm{Ca(OH)_2}]$, the chemical potential of $Ca(OH)_2$ by assuming equilibrium with HA and again using Eq. (2.3).

Now it is possible to place bounds on the value of $\mu[\mathrm{Ca_3(PO_4)_2}]$ in equilibrium conditions by considering appropriate reference systems. The reservoir must be stable with respect to formation of other calcium phosphate phases. Therefore, the $\mu[\mathrm{Ca_3(PO_4)_2}]$ of the reservoir must be less than or equal to that of β-tricalcium phosphate (β-TCP) – the low temperature stable phase – leading to a constraint

$$\mu[\mathrm{Ca_3(PO_4)_2}] \le \mu[\mathrm{Ca_3(PO_4)_2}]_{\beta-\mathrm{TCP}}$$

By calculating the total energy of a β-TCP unit cell and dividing it by the number of formula units per cell, the $\mu[\mathrm{Ca_3(PO_4)_2}]_{\beta-\mathrm{TCP}}$ at zero temperature and pressure can be found. Also, for the surfaces to exist, the HAP bulk must itself be stable against decomposition into other phases. Here, the authors consider the possibility of a decomposition of HAP into bulk $Ca(OH)_2$, while $Ca_3(PO4)_2$ is lost to the reservoir. In order to prevent this, the chemical potential of HAP must satisfy a constraint

$$\mu[\mathrm{HAP}] \le 3\mu[\mathrm{Ca_3(PO_4)_2}] + \mu[\mathrm{Ca(OH)_2}]_{bulk}$$

The first constraint gives an upper limit for HAP surfaces and the second one gives a lower limit for $\mu[\mathrm{Ca_3(PO_4)_2}]$, which provides a window for acceptable values.

When the surface energies are plotted as a function of $\mu[\mathrm{Ca_3(PO_4)_2}]$(Fig. 23), the stoichiometric (001) is found to have the lowest surface energy over a wide range of chemical potentials, although this value is somewhat higher than the 0.054 eV/Å^2 value reported by Rulis et al. [26] calculated using different methods (see below). At high values of $\mu[\mathrm{Ca_3(PO_4)_2}]$, the Ca-rich (010) becomes favorable, while at low values, the PO_4-rich (010) is favored. However, the range of values where these nonstoichiometric surfaces are stable is outside the window of stability defined by bulk HAP, $Ca(OH)_2$, and β-TCP. The stoichiometric (010) and (101) surfaces always have higher energies than stoichiometric (001). The lower energy of the (001) may be related to the coordination of O atoms in the top layer, as discussed in this Astala paper [24].

As for atomic relaxation in this Astala model – the (001) surface showed only minor relaxation with the dominant effect being a collective motion of ions in the normal direction, probably to reduce the surface electric dipole. The relaxed stoichiometric (010) and (101) surfaces exhibited a larger spread of P-O bond lengths than the bulk HAP. Similar features were found on the nonstoichiometric (010) surfaces with P-O bond lengths of 1.54–1.66 Å. The top OH groups on the (101) surface underwent about 90° rotation to become oriented perpendicular to the *c* channel direction so that the outermost surface layers are close to symmetry equivalent.

Similar detailed studies based on this approach were performed in Astala et al. work [24] for water molecules adsorption and Ca atom loss. It is important to note that in vacuum, the (001) surface is the most stable.

Another important result is that, it is possible to obtain a connection between surface charges, determined by changes of main charged groups (Ca^+ and PO_4^-), and surface energy for different surfaces and corresponding models of perfect HAP surfaces. It is very important for prospective experimental investigations.

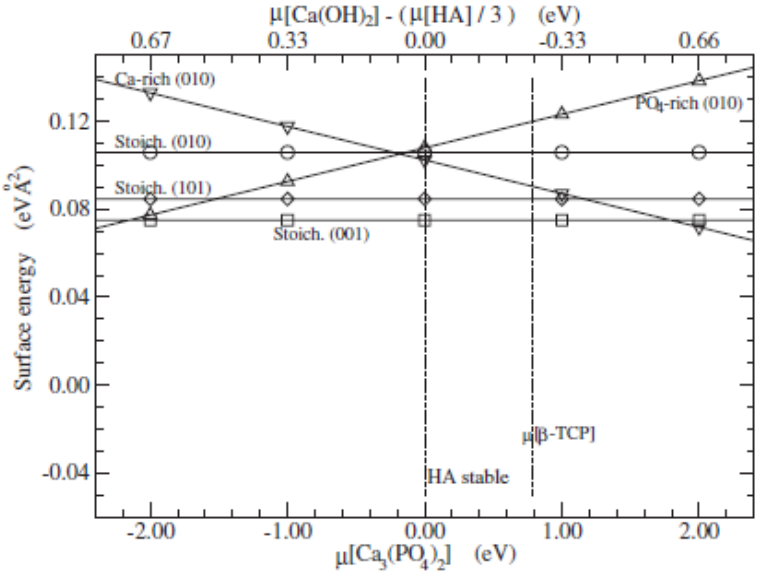

Fig. 23. The surface energies as a function of $Ca_3(PO_4)_2$ chemical potential in vacuum: squares, stoichiometric (001); circles, stoichiometric (010); diamonds, stoichiometric (101); up triangles, PO_4-rich (010); and down triangles, Ca-rich (010). For the (001) and (101) surfaces, the energy is the average over two OH polarizations. The top *x* axis shows the corresponding $Ca(OH)_2$ chemical potential, calculated using Eq. (2.3) (printed with permission from APS and Copyright Clearance Center [24]).

The results for H_2O adsorption show that all the surfaces react strongly with water because of exposed under-coordinated O atoms. The (010)-type surfaces were found to be the most reactive while (001) was the least reactive with H_2O. After adsorption of a single H_2O per cell, both (001) and Ca-rich (010) surfaces were stable, depending on the chemical environment. Wulff plots using the calculated surface energies suggest that the equilibrium shape of an HAP crystallite changes systematically as water is absorbed. The surface energy of the (010) face decreases with respect to that of the (001), and the (010) faces become more exposed as the number of adsorbed H_2O molecules increases. The Ca-rich (010) face is of particular interest. At the HAP edge of the stability window, the surface energy of this face is seen to be very similar to that of the stoichiometric (010) face, but at the other β-TCP edge, the surface energy is much lower so that for two adsorbed H_2O, the equilibrium crystallite is elongated along the *c* axis with an aspect ratio of about 2. This may be related to the morphology of HAP crystallites grown in aqueous media, and, perhaps, also to the nature of

the HAP platelets found in natural bone. Ca loss in exchange for two H was very favorable energetically. The ion release may have interesting consequences on the bioactivity.

The identification of stable surface structures and the role of H_2O adsorption give a promising starting point for future investigations, such as the studies of impurities and adsorption of different molecules. These investigations can be a basic platform for studies of other surface defects and irregularities, important for applications such as formation of various types of electric fields and electrostatic potentials distribution in the surrounding medium.

Rulis et al. [26] used some simple way, they attempted a total of four (001) surface models for HAP with different surface cuts. The relaxed total energies of the models with different cuts vary quite significantly, with differences ranging from 0.35 to 2.09 eV in HAP (001). However, the one with the lowest energy in HAP the same surface cut. Accordingly, they were adopted as the HAP (001) surface models. Omitting gross details of other surface models and construction techniques (which are available to interested parties via direct contact with the authors [26]), they present the surface energies E_{surf} , which were calculated according to

$$E_{surf} = (E_{(001)} - 2E_{cry}) / 2A, \tag{2.4}$$

where $E_{(001)}$ and E_{cry} are the total energies of the surface model and bulk crystal, respectively, and A is the surface area. The authors adopted the strategy of approximating Gibb's free energy by the total energy from the DFT calculation and ignored the influence of different chemical potentials.

This approximation is reasonable considering that the slab models are stoichiometric in this case without the addition or subtraction of any atoms to the formula unit. Note also that because the upper and lower surfaces of HAP (001) are not identical (due to the OH group orientation), the authors finally calculated the average formation energies of the two surfaces in reaction. The resulted calculated surface energy for HAP (001) according to Eq. (2.4) is therefore in average 0.871 J/m^2, or 0.0544 eV/Å^2.

The authors also tested the sensitivity of the results to the model size and found that by doubling the size of the (001) surface mode, the change in surface energy is less than 0.02 J /m^2 or 0.00125 eV/Å^2. They noted that the surface energy obtained also depends on the local density approximation (LDA) potential used [26]. Because there are no direct experimental data of surface energy measurements of clean HAP crystals in vacuum the authors try to compare the calculated surface energies with the similar oxides and argued that it had the same order of magnitudes as in other oxides. For example, Kanakis et al. [71] reported the measured surface energy of the HAP nuclei growing on oxadiazole homopolymer to be 0.158 J /m^2, a factor of 5 less than the calculated surface energy for a clean surface in vacuum.

Slepko & Demkov [22, 23, 67] used a different approach. It seems to be the most effective technique, which at least leads directly to relations of the HAP surface structure features , the changes of atomic content and positions, and corresponding surface charges, and, finally to the resulted work function. The primitive unit cell of HAP consists of 44 atoms: four atomic species that form two OH, six PO_4 groups, and ten Ca atoms per cell. Thus, to simplify the description, one must consider the crystal to be composed of these three building elements. To estimate the surface energy the authors usually use the Gibbs free energy formalism [67] with some variations. This approach allows for comparison of structures with different stoichiometry. The surface energy is given and used in [22, 23] by the equation:

$$\sigma = \left[E_{slab} - \sum_i N_i \mu_i \right] / 2A. \tag{2.5}$$

Here E_{slab} is the energy of the slab computed from first principles and μ_i and N_i are the chemical potential and number of the i-th building element, respectively. A is the surface area of the slab, the factor of two accounts for two surfaces per slab. Assuming thermodynamic equilibrium of the surface with the HAP bulk imposes the following condition:

$$\sum_i N_i \mu_i = \mu_{\mathrm{HAP}}, \tag{2.6}$$

where μ_{HAP} is the chemical potential of the HAP bulk phase, which we take equal to the bulk energy. Referencing the chemical potentials of the building elements to the corresponding bulk phases $\mu_i = \mu_i + \mu_{i,bulk}$, equation (2.6) can be rewritten as:

$$\sum_i N_i \mu_i = -E_f \ . \tag{2.7}$$

Here E_f is the formation energy. The chemical potential of Ca is reference to bulk metallic Ca. For OH and PO_4 molecules the energy per corresponding isolated molecule was used as a reference. The calculated formation energy in these works [22, 23, 67] is of –111.7 eV per $Ca_{10}(PO_4)_6(OH)_2$ molecular unit and it is in qualitative agreement with the experimental heat of formation of –138.9 eV [67, 72]. The surface energy is then estimated as:

$$\sigma = \left[E_{slab} - N_{\mathrm{Ca}}(E_{\mathrm{Ca}} + \mu_{\mathrm{Ca}}) - N_{\mathrm{OH}}(E_{\mathrm{OH}} + \mu_{\mathrm{OH}}) - N_{\mathrm{PO_4}}(E_{\mathrm{PO_4}} + \mu_{\mathrm{PO_4}}) \right] / 2A. \tag{2.8}$$

The range of chemical potentials is determined by relation, which is similar to relation (2.3) from Astala paper [24]:

$$10\mu_{\mathrm{Ca}} + 2\mu_{\mathrm{OH}} + 6\mu_{\mathrm{PO_4}} = -E_f \ , \ -E_f < \mu_i < 0. \tag{2.9}$$

With these boundary conditions we calculate the surface energy. Table 7 lists the surface energy of each model averaged over the entire chemical range. In Fig. 24 the averaged surface energy is plotted as a function of the bulk ionic charge.

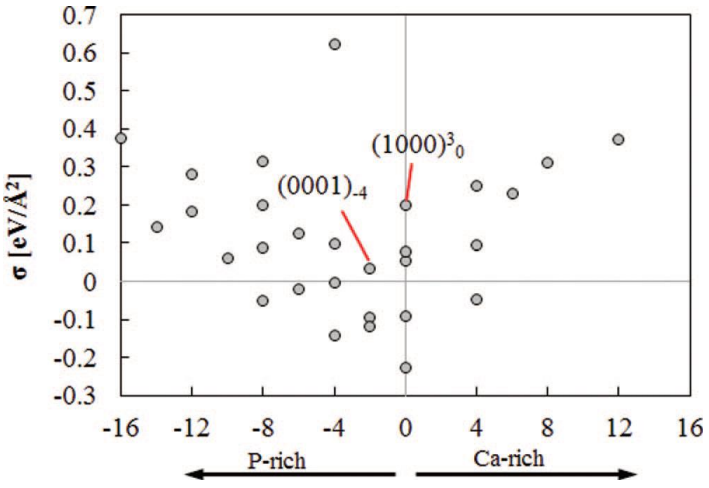

Fig. 24. Surface energy averaged over the entire chemical range plotted as a function of the stoichiometry of the models. Negative stoichiometry indicates P–rich conditions, while positive stoichiometry indicates Ca-rich models. The models $(0001)_{-4}$ and $(1000)^3_0$ are most stable under OH-rich conditions (printed with permission from AIP Publishing LLC and Copyright Clearance Center [23]).

With increasing of ionic charge and the deviation from bulk stoichiometry the surface energy increases. Here we must emphasize and remember that the large ionic charge obtained

by the authors indicates that the surface strongly deviates from HAP stoichiometry. This leads to under-coordinated functional groups Ca, OH and PO_4. It should be pointed out that while overall considered these models have a neutral charge, however, under-coordinated functional groups on the surface create additional surface dipoles that in turn increase the slab energy.

The surface energy ranges between -0.23 eV/Å^2 and $+0.62$ eV/Å^2. To interpret the data the authors [23, 67] assumed that this is a relative energy rather than its absolute value (this reflects the arbitrary choice of thermodynamic references). Alternatively, the negative energy may be interpreted in this case as the surface being more stable than the bulk, which would suggest etching under the certain choices of chemical reference potentials and therefore unstable under given conditions. The obtained here stoichiometric $(0001)_0$ and $(1000)_0^2$ surfaces have energy 0.055 eV/Å^2 and 0.076 eV/Å^2, respectively, in good agreement with the 0.075 eV/Å^2 and 0.105 eV/Å^2 reported by Astala et al.[24], and the 0.054 eV/Å^2 reported by Rulis et al.[26] for the $(0001)_0$ (or (001)) orientation. Furthermore, the stoichiometric $(1000)_0^1$ and $(1000)_0^3$ models correspond to Astala's PO_4-rich and Ca-rich surfaces, respectively. Astala calculates the surface energy with respect to the β-tricalcium phosphate (β-TCP) with the formula units $Ca_3(PO_4)_2$ and $Ca(OH)_2$. These two references are reasonable choices; however, it must be noted that in practice they greatly reduce the number of allowed surface terminations. Resulted Astala's surface energies are 0.11 eV/Å^2 and 0.10 eV/Å^2 for the PO_4-rich and Ca-rich surfaces, respectively, averaged over the allowed chemical potential range. Slepko&Demkov [23, 67] found the average values 0.05 eV/Å^2 and 0.06 eV/Å^2 for these two surfaces with respect to $Ca_3(PO_4)_2$ and $Ca(OH)_2$. Such deviation between Slepko&Demkov and Astala's works could be attributed to the difference in their methods of constructing the HAP surface.

While in [23] the surface models are constructed in a quasi-symmetric way as described earlier to suppress macroscopic electric fields across the slab, Astala's surface models are terminated stoichiometrically on one side and with the termination of interest on the other side. This inevitably creates an electric field across the slab and modifies the surface energy. Note, that all these models have zero bulk ionic charge as it was earlier pointed out by all the authors. The most important results of the work [23, 67] are the direct calculations of the work function.

3.4. Electron work function (from data of the HAP DFT modeling)

A very important question is how the surface structure and composition influence the work function of HAP. The work function is one of several key parameters determining charge transfer at the material's interface. In photoelectron emission measurements, the work function is found to range between 4.7 eV and 5.1 eV [30, 48] and to correlate with the size of the HAP particles used for the measurement and with concentration of hydrogen atoms at the surface [30].

Surprisingly, the work function ranges between 10 and 3 eV, depending on the specific model used. To gain further insight, Fig. 25 shows the work function as a function of the bulk ionic charge in the surface slab (note that as before, this reflects the stoichiometry of the model which is overall neutral).

A negative ionic charge indicates that the model contains unbalanced PO_4^{3-} and OH^{1-} groups. Positive net ionic charge means that the surface contains unbalanced Ca^{2+}. The plot reveals that the large variation in the work function can be traced to a significant variation at the surface in the concentration of Ca and PO_4 groups. The energy levels of valence 4*s* electrons in Ca are relatively close to vacuum, leading to the low work function of 2.9 eV for bulk Ca metal. On the other hand, the occupied orbitals of a covalently bonded PO_4 group have very low energy. Thus, in the Ca-rich surface models the work function tends to be close to that of bulk Ca, while in the PO_4-rich models it varies between 7 eV and 10 eV. This is

what one would expect for the anti-bonding states of PO_4 groups (the energy of the sp^3–hybrid in phosphorus is –10.5 eV and the *p*-orbital of oxygen is at –14.3 eV, with respect to vacuum). The work function of the two surface models most stable under OH-rich conditions (model $(0001)_{-4}$ and $(1000)^3_0$) is pointed out by the large circles in Fig. 25. For model $(0001)_{-4}$ the value of 7.5 eV was found. Interestingly, for model $(1000)^3_0$ the value of 5.1 eV was found which is in the closest agreement with the experimental value [15, 30, 48]. This again suggests that it may be a good model for the OH-terminated HA surface described by Sato et al. [23, 67, 75].

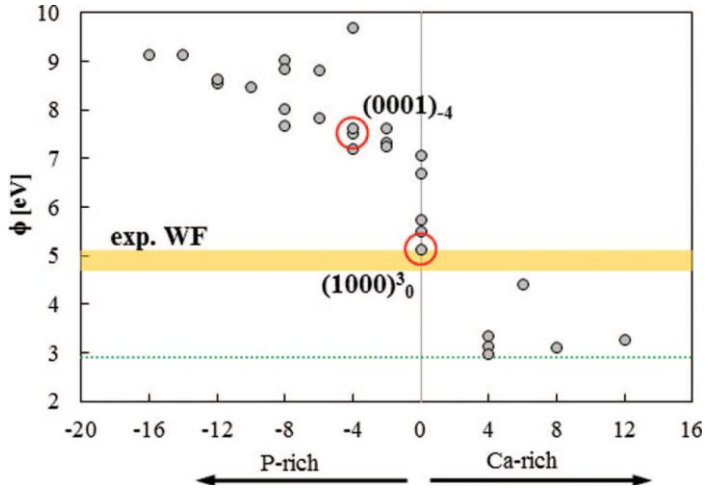

Fig. 25. Work function as a function of the stoichiometry of the models. Negative stoichiometry indicates P-rich conditions, while positive stoichiometry indicates Ca-rich models. The authors of [23] point out the models $(0001)_{-4}$ and $(1000)^3_0$ which are most stable under OH-rich conditions. The work function strongly depends on the stoichiometry, ranging from 3 eV to 9.5 eV. The range of experimental work function is indicated by the shaded bar (printed with permission from AIP Publishing LLC and Copyright Clearance Center [23]).

The results obtained allow us to carry out further targeted study of the design of nanostructures HAP surface with desired electrical properties – charges, electric field and potential, and could serve a tool to control the electron work function. Currently, this result, in our opinion, is one of the most important ones because it shows direct connection between construction and content of the surface of initially perfect HAP structures and the corresponding work function. This gives experimenters a chance to change the HAP surface, if they want to reach some specific desirable value of the work function. Besides they can assess how this value of the work function can be obtained by targeted reconstruction of HAP surfaces. Finally we must only bear in mind that in the last approach the consideration was given to the thermoelectronic work function, but not to the photoelectron emission work function. These values differ by shift from Fermi level *F* with respect to the valence band top E_v, for excited by photons and emitted electrons. But it is possible to take it into account in experimental conditions and measurements by available technique, and thus calculate the necessary shift of energy.

CONCLUSIONS

Using the density functional theory, a comprehensive study of the vacuum-cleaved surface of important biomineral HAP was considered in this review. The study is a first step in considering interfaces of HAP with any surface, such as Ti and TiO_2 which are important in biomedical applications as implants. Considering a wide range of surface compositions and orientations, here the stoichiometry was identified as the main origin of the increase in the

vacuum-cleaved surface energy. For the biologically relevant OH-rich environment two dominant surface structures were found, one with the (0001) orientation and one with the (1000) orientation. The (1000) surface has OH groups directly facing vacuum. The surface undergoes major reconstruction to stabilize the OH groups.

The estimated work function of HAP is found to range from 3.0 eV for the Ca-rich termination to 9.7 eV for Ca-poor surfaces. The work function of the OH-terminated surface is 5.1 eV, which is in very good agreement with the experimentally reported values that range from 4.7 eV to 5.1 eV [15, 30 and 48]. The models developed and results obtained suggest the following statements.

1) The models of HAP clusters and NPs developed reveal the main features of the HAP crystal formation and rise, allow us to describe their properties and predict the arising electrical charges and potential both inside the crystal and in the surrounding medium.

2) The models constructed and the first principle and DFT approaches developed for computational studies of the bulk HAP with a perfect structures and with the embedded various defects allow calculating their new properties and apply them in prospective investigations.

3) The models constructed and the first principle and DFT approaches developed for computational studies of the HAP surface with ideal structures and therefore regular stoichiometry reveal their properties and peculiarities, which are necessary for experimental studies.

4) A basis for calculations and prediction of the properties for the HAP surface can be created with any and not-ideal imperfect structures, including any defects in various types of the HAP surfaces, based on the developed various types of the supercell models with vacuum inter-layers, which are most important for further studies and practical applications.

5) The new models developed for oxygen deficiency in the phosphate groups gives an explanation of the photocatalytic activity of HAP observed in this material under UV light and open new prospectives for HAP application in environmental remediation and bacteria inactivation.

These studies were supported by The Russian Foundation for Basic Research (grant number 15-01-04924).

REFERENCES

1. Kay M.I., Young R.A., Posner A.S. Crystal Structure of Hydroxyapatite. *Nature* (*London*). 1964. V. 204. P. 1050.
2. Elliot J.C. *Structure and Chemistry of the Apatites and Other Calcium Orthophosphates*. Amsterdam: Elsevier, 1994.
3. *Biomaterial Science*. Ed. Rather B.D. London: Academic Press, 1996.
4. Hughes J.M., Cameron M., Crowley K.D. Structural variations in natural F, OH, and Cl apatites. *American Mineralogist*. 1989. V. 74. P. 870–876. URL: http://rruff.geo.arizona.edu/AMS/result.php (accessed: 21.12.2016).
5. Elliot J.C., Mackie P.E., Young R.A. Monoclinic hydroxyapatite. *Science*. 1973. V. 180. No. 4090. P. 1055–1057.
6. Young R.A. Dependence of apatite properties on crystal structural details. *Trans. N. Y. Acad. Sci.* 1967. No. 7. P. 949–959.
7. Ikoma T., Yamazaki A. Preparation and Structure of Refinement of Monoclinic Hydroxyapatite. *J. Solid State Chem*. 1999. V. 144. P. 272–276.
8. Ma G., Liu X.Y. Hydroxyapatite: Hexagonal or Monoclinic? *Crystal Growth & Design.* 2009. V. 9. No. 7. P. 2991–2994.
9. Calderin L., Stott M. J., Rubio A. Electronic and crystallographic structure of apatites. *Phys. Rev. B.* 2003. V. 67. P. 134–106.

10. Tofail S.A.M., Haverty D., Stanton K.T., Mcmonagle J.B. Structural Order and Dielectric Behaviour of Hydroxyapatite. *Ferroelectrics*. 2005. V. 319. P. 117–123.
11. Hitmi N., LaCabanne C., Young R.A. OH^- dipole reorientability in hydroxyapatites: effect of tunnel size. *J. Phys. Chem. Solids*. 1986. V. 47. No. 6. P. 533–546.
12. Nakamura S., Takeda H., Yamashita K. Proton transport polarization and depolarization of hydroxyapatite ceramics. *J. Appl. Phys.* 2001. V. 89. No. 10. P. 5386–5392.
13. Bystrov V.S., Paramonova E.V., Bystrova N.K., Sapronova A.V. Hydroxyapatite polarization properties. *Scientific Proceedings of Riga Technical University: Material Sciences and Applied Chemistry*. 2008. V. 17. No. 1. P. 30–37.
14. Bystrov V.S., Bystrova N.K., Paramonova E.V., Dekhtyar Yu.D. Interaction of charged hydroxyapatite and living cells. I. Hydroxyapatite polarization properties. *Mathematical biology and Bioinformatics*. 2009. V. 4. No. 2. P. 7–11.
15. *PERCERAMICS: Multifunctional percolated nanostructured ceramics fabricated from hydroxyapatite*. NMP3-CT-2003-504937 FP6 project. Riga Technical University. 2007. URL: http://cordis.europa.eu/publication/rcn/12743_en.html (accessed 21.12.2016).
16. Epple M., Ganesan K., Heumann R., Klesing J., Kovtun A., Neumann S., Sokolova V. Application of calcium phosphate nanoparticles in biomedicine. *Journal of Materials Chemistry*. 2010. V. 20. No. 1. P. 18–23.
17. Dorozhkin S.V. Nanosized and nanocrystalline calcium orthophosphates. *Acta Biomaterialia*. 2010. V. 6. P. 715–734.
18. Leon B., Janson J.A. *Thin Calcium Phosphate Coatings for Medical Implants.* Springer, 2009.
19. de Leeuw N.H. Computer simulations of structures and properties of the biomaterial hydroxyapatite. *J. Mater. Chem.* 2010. V. 20. P. 5376–5389. doi: 10.1039/B921400C.
20. Haverty D., Tofail S.A.M., Stanton K.T., McMonagle J.B. Structure and stability of hydroxyapatite: Density functional calculation and Rietveld analysis. *Phys. Rev. B.* 2005. V. 71. P. 094103.
21. Mostafa N.Y., Brown P.W. Computer simulation of stoichiometric hydroxyapatite: Structure and substitutions. *J. Physics and Chemistry of Solids*. 2007. V. 68. No. 3. P. 431–437.
22. Slepko A., Demkov A.A. First-principles study of the biomineral hydroxyapatite. *Phys. Rev. B.* 2011. V. 84. P. 134–108.
23. Slepko A., Demkov A.A. First-principles study of hydroxyapatite surface. *J. Chem. Phys.* 2013. V. 139. P. 044714.
24. Astala R., Stott M.J. First-principles study of hydroxyapatite surfaces and water adsorption. *Phys. Rev. B.* 2008. V. 78. P. 075427.
25. Rulis P., Ouyang L., Ching W.Y. Electronic structure and bonding in calcium apatite crystals: hydroxyapatite, fluoapatite, chlorapatite and bromapatite. *Phys. Rev. B.* 2004. V. 70. P. 155–104.
26. Rulis P., Yao H., Ouyang L., Ching W.Y. Electronic structure, bonding, charge distribution, and x-ray absorption spectra of the (001) surfaces of fluorapatite and hydroxyapatite from first principles. *Phys. Rev. B.* 2007. V. 76. P. 245–410.
27. Matsunaga K., Kuwabara A. First-principles study of vacancy formation in hydroxyapatite. *Phys. Rev. B.* 2007. V. 75. P. 014102.
28. Bystrov V., Paramonova E., Bystrova N., Sapronova A., Filippov S. Computational molecular nanostructures and mechanical/adhesion properties of Hydroxyapatite. In: *Micro- and Nanostructures of Biological Systems.* Ed. G. Bischoff. Martin Luther University Halle-Wittenberg. Aachen: Shaker Verlag, 2005. P. 77–93.
29. Bystrov V., Bystrova N., Paramonova E., Sapronova A., Filippov S. Modeling and computation of Hydroxyapatite nanostructures and properties. *Advanced materials forum III. Mater. Science Forum.* 2006. V. 514-516. No. 1-2. P. 1434–1437.

30. Bystrov V. S., Paramonova E., Dekhtyar Y., Katashev A., Karlov A., Polyaka N., Bystrova A. V., Patmalnieks A., Kholkin A. L. Computational and experimental studies of size and shape related physical properties of hydroxyapatite nanoparticles. *J. Phys.: Cond. Matter.* 2011. V. 23. P. 065302.
31. Bystrov V., Costa E., Santos S., Almeida M., Kholkin A., Kopyl S., Dekhtyar Yu., Bystrova A.V., Paramonova E.V. Computational Study of Hydroxyapatite Properties and Surface Interactions. *IEEE Conf. Publications*. 2012. P. 1–3. doi: 10/1109/ISAF.2012.6297766.
32. Bystrov V.S., Paramonova E.V., Costa M.E.V., Santos C., Almeida M., Kopyl S., Dekhtyar Yu., Bystrova A.V., Maevsky E.I., Pullar R.C. and Kholkin A.L. Computational Study of the Properties and Surface Interactions of Hydroxyapatite. *Ferroelectrics.* 2013. V. 449. No. 1. P. 94–101. doi: 10.1080/00150193.2013.822774.
33. Bystrova A.V., Dekhtyar Yu.D., Popov A.I., Bystrov V.S. Modeling and synchrotron data analysis of modified Hydroxyapatite structure. *Mathematical Biology and Bioinformatics.* 2014. V. 9. No. 1. P. 171–182.
34. Bystrova A.V., Dekhtyar Yu.D., Popov A.I., Coutinho J., Bystrov V.S. Modified Hydroxyapatite Structure and Properties: Modeling and Synchrotron Data Analysis of Modified Hydroxyapatite Structure. *Ferroelectrics.* 2015. V. 475. No. 1. P. 135–147. doi: 10.1080/00150193.2015.995580.
35. Bystrov V.S., Coutinho J., Bystrova A.V., Dekhtyar Yu.D., Pullar R.C., Poronin A., Palcevskis E., Dindune A., Alkan B., Durucan C., Paramonova E.V. Computational study of the hydroxyapatite structures, properties and defects. *J. Phys. D: Appl. Phys*. 2015. V. 48. P. 195–302.
36. Dekhtyar Yu., Khlusov I., Polyaka N., Sammons R., Tyulkin F. Influence of Bioimplant Surface Electrical potential on osteoblast Behaviour and Bone Tissue Formation. In: *IFMBE Proc. 12th Mediterranean Conference on Medical and Biological Engineering and Computing*. Eds. Bamidis P.D. and Pllikarakis N. Munich: MEDICON. 2010. V. 29. P. 800–803.
37. Dekhtyar Yu., Polyaka N., Sammons R. Electrically Charged Hydroxyapatite Enhances Immobilization and Proliferation of Osteoblasts. In: *IFMBE Proceedings*. Eds. Katashev A., Dekhtyar Yu., Spigulis J. Berlin Heidelberg: Springer-Verlag, 2008. V. 20. P. 23–25.
38. Dekhtyar Yu., Bystrov V., Bystrova A., Dindune A., Katashev A., Khlusov I., Palcevskis E., Paramonova E., Polyaka N.N., Romanova M., Sammons R., Veljović D. Engineering of the Hydroxyapatite Cell Adhesion Capacity. In: *IFMBE Proceedings:* International Symposium on Biomedical Engineering and Medical Physics. (10–12 October 2012. Latvia, Riga). Ed. Dekhtyar Yu. Heidelberg: Springer, 2013. V. 38. P. 182–185.
39. Dehtjars J., Dvornichenko M., Karlov A., Khlusov I., Poļaka N., Sammons R., Zajcevs K. Electrically Functionalized Hydroxyapatite and Calcium Phospate Surfaces to Enhance Immobilization and Proliferation of Osateoblasts In Vitro and Modulate Osteogenesis In Vivo. In: *IFMBE Proceedings:* World Congress on Medical Physics and Biomedical Engineering. (Germany, Munich. 2009). Eds. Dossel O and Schlegel W.C. Berlin: Springer, 2010. V. 25. No. 10. P. 245–248. doi: 10.1007/978-3-642-03900-3_70.
40. Dekhtyar Yu., Bystrov V., Khlusov I., Polyaka N., Sammons R., Tyulkin F. Hydroxyapatite Surface Nanoscaled characterization and Electrical Potential Functionalization to Engineer Osteoblasts Attachment and Generate Bone Tissue. In: *Society For Biomaterials Annual Meeting:* book of abstracts (11–16 April, 2011. Orlando, Florida, USA). Abstract No. 519.

41. Onuma K. Recent research on pseudobiological hydroxyapatite crystal growth and phase transition mechanisms. *Progress in Crystal Growth and Characterization of Materials.* 2006. V. 52. P. 223–245.
42. Yin X., Scott M. J. Biological calcium phosphates and Posner´s cluster. *J. Chem. Phys.* 2003 V. 118. No. 8. P. 3717–3723.
43. Bystrov V.S. Piezoelectricity in the Ordered Monoclinic Hydroxyapatite. *Ferroelectrics.* 2015. V. 475. No. 1. P. 148–153. doi: 10.1080/00150193.2015.995581.
44. Menendez-Proupin E., Cervantes-Rodriguez S., Osorio-Pulgar R., Franco-Cisterna M., Camacho-Montes H. and Fuentes M.E. Computer simulation of the elastic constants of hydroxyapatite and fluorapatite. *J. Mechanical Behavior of Biomedical Materials*. 2011. V. 4. P. 1011–1020.
45. Martins M., Santos C., Almeida M., Costa E. Hydroxyapatite micro- and nanoparticles: Nucleation and growth mechanisms in the presence of citrate species. *J. Colloid and Interface Science*. 2008. P. 210–216.
46. Ye F., Guo H., Zhang H. Biomimetic synthesis of oriented hydroxyapatite mediated by nonionic surfactants. *Nanothechnology.* 2008. V. 19. No. 24. P. 245606.
47. Aronov D., Chaikina M., Haddad J., Karlov A., Mezinskis G., Oster L., Pavlovska I., Rosenman G. Electronic states spectroscopy of Hydroxyapatite ceramics. *J. Mater. Sci: Mater. Med*. 2007. V. 18. P. 865–870.
48. Bystrov V., Bystrova N., Dekhtyar Yu. Size depended electrical properties of Hydroxyapatite nanoparticles. In: *IFMBE Proceedings 25/ VIII. WC 2009.* Eds. O. Dossel and W.C. Schlegel. Berlin: Springer, 2009. P. 230–232.
49. Bystrov V.S., Dekhtyar Yu., Paramonova E., Pullar R., Katashev A., Polyaka N., Bystrova A.V., Sapronova A., Fridkin V., Kliem H., Kholkin A.L. Polarization of PVDF and P(VDF – TrFE) thin films revealed by emission spectroscopy with computational simulation during phase transition. *J. Appl. Phys.* 2012. V. 111. P. 104113. doi: 10.1063/1.4721373.
50. Lang S.B., Tofail S.A.M., Gandhi A.A., Gregor M., Wolf-Brandstetter C., Kost J., Bauer S., Krause M. Pyroelectric, piezoelectric, and photoeffects in hydroxyapatite thin films on silicon. *Appl. Phys. Lett*. 2011. V. 98. P. 123703.
51. Lang S.B., Tofail S.A.M., Kholkin A., Wojtas M., Gregor M., Gandhi A., Wang Y., Bauer S., Krause M., Plecenik A. Ferroelectric polarization in nanocrystalline hydroxyapatite thin films on silicon. *Sci. Rep.* 2013. V. 3. P. 2215.
52. *AIMPRO Home Page*. URL: http://aimpro.ncl.ac.uk/ (accessed 11.12.2016).
53. Britney P.R., Jones R. LDA Calculations Using a Basis of Gaussian Orbitals. *Phys. Status Solidi B: Basic Res.* 2000. V. 217. P. 131–171.
54. Briddon P.R., Rayson M.J. Accurate Kohn–Sham DFT with the Speed of Tight Binding: Current Techniques and Future Directions in Materials Modeling. *Phys. Status Solidi B.* 2011. V. 248. No. 6. P. 1309–1318.
55. *HyperChem. Tools for Molecular Modeling* (release 7, 8). Professional edition. Gainesville: Hypercube, Inc., 2002. URL : http://www.hyper.com/?TabId=385 (accessed 28.12.2016).
56. Stewart J.J.P. Optimization of parameters for semi-empirical methods I. Method. *J. Comp. Chem.* 1989. V. 10. No. 2. P. 209–220. II. Applications. P. 221–264.
57. Terpstra R.A., Bennema P., Hartman P., Woensdregt C.F., Perdok W.G., Senechal M.L. F faces of apatite and its morphology: theory and observation. *J. Crystal Growth.* 1986. V. 78. P. 468–478.
58. Wenge Jiang, Haihua Pan, Yurong Cai, Jinhui Tao, Peng Liu, Xurong Xu, Ruikang Tang. Atomic Force Microscopy Reveals Hydroxyapatite-Citrate Interfacial Structure at the Atomic Level. *Langmuir.* 2008. V. 24. P. 12446–12451.
59. Hu Y.-Y., Rawal A., Schmidt-Rohr K. Strongly bound citrate stabilizes the apatite nanocrystals in bone. *PNAS.* 2010. V.107. No. 52. P. 22425–22429.

60. Vandiver J., Dean D., Patel N., Bonfield W., Ortiz C. Nanoscale variation in surface charge of synthetic hydroxyapatite detected by chemically and spatially specific high-resolution force spectroscopy. *Biomaterials*. 2005. V. 26. P. 271–283.
61. Horiuchi N., Nakaguki S., Wada N., Nozaki K., Nakamura M., Nagai A., Katayama K., Yamashita K. Polarization-induced surface charges in hydroxyapatite ceramics. *J. Appl. Phys*. 2014. V. 116. P. 01490.
62. Johann F. and Soergel E. Quantitative measurement of the surface charge density. *Appl. Phys. Lett*. 2009. V. 95. P. 232906. doi: 10.1063/1.3269606
63. Bystrov V.S., Seyedhosseini E., Kopyl S., Bdikin I., Kholkin A. Piezoelectricity and ferroelectricity in biomaterials: Molecular modeling and piezoresponse force microscopy measurements. *J. Appl. Phys*. 2014. V. 116. No. 6. P. 066803.
64. Bystrov V.S., Bdikin I., Heredia A., Pullar R.C., Mishina E., Sigov A.S., Kholkin A.L. Piezoelectricity and Ferroelectricity in Biomaterials: From Proteins to Self-assembled Peptide Nanotubes. In: *Piezoelectric Nanomaterials for Biomedical Applications*. Eds. Ciofani G., Menciassi A. Berlin Heidelberg: Springer-Verlag, 2012. Chapter 7. P. 187–211.
65. Halperin C., Mutchnik S., Argonin A., Molotski M., Urenski P., Salai M., Rosenman G. Piezoelectric effect in Human Bones Studied in Nanometer Scale. *Nano Lett*. 2004. V. 4. No. 7. P. 1253–1256.
66. Kittel C. *Introduction to solid state physics.* New York: J. Wiley and Sons, Inc., 1978.
67. Slepko A. *Theory of Biomineral Hydroxyapatite:* PhD Thesis. 160 pages. University of Texas at Austin, 2013.
68. *VASP (Vienna Ab initio Simulation Package)* URL: https://www.vasp.at/ (accessed 22.11.16)
69. Hollinger J.O., Einhorn T.A., Doll B., Sfeir C. *Bone Tissue Engineering*. Washington: CRC Press, 2004. P. 91.
70. Yamashita K., Oikawa N., Umegaki T. Acceleration and Deceleration of Bone-Like Crystal Growth on Ceramic Hydroxyapatite by Electric Poling. *Chem. Mater.* 1996. V. 8. P. 2697.
71. Kanakis J., Chrissanthopoulos A., Tnaetos N., Kallitsis A., Dalas E. Crystallization of Hydroxyapatite on Oxadiazole-Based Homopolymers. *Cryst. Growth Des*. 2006. V. 6. P. 1547. doi: 10.1021/cg060015u
72. Cruz F.J.A.L., Minas da Piedade M.E., Calado J.C.G. Standard molar enthalpies of formation of hydroxy-, chlor-, and bromapatite. *J. Chem. Thermodynamics.* 2005. V. 37. P. 1061. doi: 10.1016/j.jct.2005.01.010
73. Bystrov V.S., Piccirillo C., Tobaldi D.M., Castro P.M.L., Coutinho J., Kopyl S., Pullar R.C. Oxygen vacancies, the optical band gap (E_g) and photocatalysis of hydroxyapatite: comparing modelling with measured data. *Applied Catalysis B: Environmental*. 2016. V. 196. P. 100–107. doi: 10.1016/j.apcatb.2016.05.014.
74. Bystrov V.S., Pullar R.C., Kopyl S., Piccirillo C., Coutinho J. Computational Studies of the Vacancies in Hydroxyapatite. In*: Book of abstracts of the 1st international Conference on Materials Design and Applications 2016 (MDA2016)*. 30 June – 1 July, 2016, Portugal. Porto: Faculty of Engineering; University of Porto, 2016. MDA16-55. P. 43.
75. Sato K., Kogure T., Iwai H., Tanaka J. Atomic-Scale {101¯0} Interfacial Structure in Hydroxyapatite Determined by High-Resolution Transmission Electron Microscopy. *J. Am. Ceram. Soc.* 2002. V. 85. P. 3054. doi: 10.1111/j.1151-2916.2002.tb00578.x

Received November 25, 2016.
Published January 16, 2017.